





Review

# Effective Strategies, Mechanisms, and Photocatalytic Efficiency of Semiconductor Nanomaterials Incorporating rGO for Environmental Contaminant Degradation

Noor Haida Mohd Kaus <sup>1,\*</sup> , Ahmad Fadhil Rithwan <sup>1</sup>, Rohana Adnan <sup>1</sup> , Mohd Lokman Ibrahim <sup>2,3</sup> , Sirikanjana Thongmee <sup>4</sup>  and Siti Fairus Mohd Yusoff <sup>5</sup>

<sup>1</sup> School of Chemical Sciences, Universiti Sains Malaysia, Gulong 11800, Penang, Malaysia; ahmadfadhil18@gmail.com (A.F.R.); r\_adnan@usm.my (R.A.)

<sup>2</sup> Faculty of Applied Sciences, Universiti Teknologi MARA, Shah Alam 40450, Selangor, Malaysia; mohd\_lokman@uitm.edu.my

<sup>3</sup> Centre for Functional Materials and Nanotechnology, Institute of Science, Universiti Teknologi MARA, Shah Alam 40450, Selangor, Malaysia

<sup>4</sup> Department of Physics, Faculty of Science, Kasetsart University, Bangkok 10900, Thailand; fscisjn@ku.ac.th

<sup>5</sup> Department of Chemical Sciences, Faculty of Science and Technology, Universiti Kebangsaan Malaysia, Bangi 43600, Selangor, Malaysia; sitifairus@ukm.edu.my

\* Correspondence: noorhaida@usm.my



**Citation:** Mohd Kaus, N.H.; Rithwan, A.F.; Adnan, R.; Ibrahim, M.L.; Thongmee, S.; Mohd Yusoff, S.F. Effective Strategies, Mechanisms, and Photocatalytic Efficiency of Semiconductor Nanomaterials Incorporating rGO for Environmental Contaminant Degradation. *Catalysts* **2021**, *11*, 302. <https://doi.org/10.3390/catal11030302>

Academic Editors: Detlef W. Bahnemann and Antonella Profumo

Received: 31 December 2020

Accepted: 17 February 2021

Published: 25 February 2021

**Publisher's Note:** MDPI stays neutral with regard to jurisdictional claims in published maps and institutional affiliations.



**Copyright:** © 2021 by the authors. Licensee MDPI, Basel, Switzerland. This article is an open access article distributed under the terms and conditions of the Creative Commons Attribution (CC BY) license (<https://creativecommons.org/licenses/by/4.0/>).

**Abstract:** The water pollution problems severely affect the natural water resources due to the large disposal of dyes, heavy metals, antibiotics, and pesticides. Advanced oxidation processes (AOP) have been developed using semiconductor nanomaterials as photocatalysts for water treatment as an essential strategy to minimize environmental pollution. Significant research efforts have been dedicated over the past few years to enhancing the photocatalytic efficiencies of semiconductor nanomaterials. Graphene-based composites created by integrating reduced graphene oxide (rGO) into various semiconductor nanomaterials enable the unique characteristics of graphene, such as the extended range of light absorption, the separation of charges, and the high capacity of adsorption of pollutants. Therefore, rGO-based composites improve the overall visible-light photocatalytic efficiency and lead to a new pathway for high-performance photocatalysts' potential applications. This brief review illustrates the strategies of combining rGO with various semiconductor nanomaterials and focuses primarily on modification and efficiency towards environmental contaminants.

**Keywords:** semiconductor; nanomaterials; reduced graphene oxide; photocatalysis

## 1. Introduction

Many environmental issues have emerged globally over the past few decades. These include climate change caused by the greenhouse effect, air pollution caused by open burning, and water pollution caused by industrial wastewater that has not properly treated. A central topic addressing specifically better treatment approaches is clean water standards of everyday life. Good water quality is needed for many uses, such as drinking and residential water sources, irrigation, infrastructure, transportation, and power supply [1]. Several indices have commonly been used to determine water quality, such as the River Habitat Survey (RHS), the Water Quality Index (WQI), and Index of contamination of water (WPI) [2]. The Ganga River in India [3], the Liao River in China [4], and the Semenyih River in Malaysia [5] are examples of water pollution around the world. The sources of contamination in the Ganga River are inorganic and organic compounds from agricultural and industrial waste, religious practices, and sewage, as reported by Chaudhary et al. [3]. In other countries, such as Putrajaya, Malaysia, where low concentrations of pharmaceutical residues were discovered in drinking water from the Semenyih River [5], some sources may also be linked to water contamination.

Long-term adverse side effects of carcinogenic contaminants such as heavy metals, dyes, persistent organic pollutants (POPs), and antibiotics are present in water sources [6]. In addition, pharmaceutical waste such as antibiotics will increase microorganisms and bacteria's resistance to antibiotics [7]. These pharmaceutical wastes typically come from insufficient water treatment facilities, hospital and industrial wastewater [8], and urine from living organisms [9]. Other than that, in our modern world, POPs are a problem because they are a recalcitrant chemical that can last long in the atmosphere and can travel long distances before being redeposited in a new area [10]. Researchers reported the existence of POPs is far away from sources in the field. Transportation, agriculture, and combustion are such sources of these chemicals. Therefore, a considerable effort has been made to eliminate these contaminants to ensure improved water quality for human consumption.

Coagulation, sedimentation, and adsorption are conventional approaches used to treat wastewater in sewage treatment plants. Coagulation is the mixture of tiny particles known as flocs, which adsorb the dissolved organic matter [11] to form larger aggregates. Adsorption, on the other hand, is a mechanism in which the mixture of substances functions as an adsorbent and adsorbate [12] at the interface of two phases of materials. These approaches are practical and are commonly used in the treatment of wastewater. These techniques, however, showed low efficiency in the treatment of pharmaceutical waste, heavy metals, and certain dyes [13] and did not reduce the problem. The adsorption process, for example, can generate secondary waste. The pollutant is only adsorbed but not mineralized to become simpler molecules such as carbon dioxide and water. Before being reused, the adsorbent used needs to be washed and regenerated. Thus, the advanced oxidation process (AOP) is an alternative method to help remove these contaminants in the traditional wastewater treatment system since it can mineralize the pollutants by redox reactions into safer compounds.

## 2. Advanced Oxidation Process

The Advanced Oxidation Process (AOP) is a method that uses oxidizing agents such as hydroxyl radical ( $\text{OH}^\bullet$ ), superoxide radical ( $\text{O}_2^{\bullet-}$ ), and sulphate radical ( $\text{SO}_4^{\bullet-}$ ) to degrade refractory pollutants in wastewater treatment plants, such as organic and inorganic matter [14]. In the 1980s, the first AOP was implemented as a drinking water-treated technique [15]. Then, for domestic use, this system continued to be used to treat wastewater treatment. The efficacy of the treatment depends on the type of AOP used, the physicochemical properties of the contaminants encountered, and the environmental parameters [14]. For the decontamination process to take place, the production of these radicals needs to be adequate.

Nevertheless, the lifetime of the generated radicals is short; hence, as the radicals' concentration is deficient, it is less suitable for other applications such as pathogen disinfection [14]. The advantages of this approach are applicable in small-scale application, [13] high and nonselective degradation [16], and rapid reaction rates [17]. This approach also helps mineralize the pollutants by forming intermediates and produce less toxic materials [18]. In most research papers, photolysis technique [19], sonolysis [20], photo-Fenton [21], and photocatalysis [22] are the most used of all advanced oxidation processes. Photocatalysis is one of AOP that creates radicals using semiconductors and light energy. The formation of electron-hole pairs and radicals can be produced when the light energy intensity is higher than the bandgap energy of the semiconductor. Nevertheless, it has been reported some of the semiconductors require modification to enhanced and sustained its photocatalytic performance towards pollutants by integrating with other materials such as polymer, graphene, or other metals. This review will focus on strategies for the construction of reduced graphene oxide (rGO)-integrated semiconductor nanomaterials and their photocatalytic performance against pollutants.

### 2.1. Semiconductor Nanomaterials as Photocatalyst

A semiconductor is a material classified as a conductor and an insulator. The examples of semiconductor are metal oxides, metal ferrites, and metal sulfides. These semiconductors have a specific bandgap consisting of the conduction band (CB) and the valance band (VB), which in each type of semiconductor differs in the distance between the gaps. The energy needed to excite the electron from the valance band to the conduction band is known as bandgap energy and is necessary for photocatalysis. Semiconductor nanomaterials have been commonly used as photocatalysts in the photocatalysis process because of their ability to use light energy and produce charged carriers [23] that are vital for various applications. Water splitting for hydrogen production [23] and water treatment for the degradation of organic and inorganic contaminants [6,24] are the example of photocatalytic applications utilizing semiconductor nanomaterials. Examples of the most used semiconductor nanomaterials in the field of photocatalysis are  $\text{TiO}_2$  [9],  $\text{ZnO}$  [25],  $\text{BiFeO}_3$  [26],  $\text{BiVO}_4$  [27],  $\text{SnO}_2$  [28], and  $\text{CdO}$  [29]. Each of the described photocatalysts has its specific bandgap range, determining whether they are UV light or visible light active materials. The wider bandgap of the materials explained the greater energy is required for the electron to be excited from the valance band (VB) to the conduction band (CB). It is important to note that the fabrication strategies such as metal doping (Au, Pt, and Ag) [30–32], heterojunction with photosensitizer materials (reduced graphene oxide (rGO) and carbon nanotubes) [33,34], and the particles size distribution are necessary to modify the bandgap energy of semiconductors.

In particular, the introduction of doping or heterojunction of metals inside the semiconductor can generate intermediate energy states in the system, and help to capture the photoinduced electron, subsequently minimizing the recombination of the electron-hole [35]. In addition, the photosensitizer materials can help transport the photoinduced electron from the conduction band away and can increase its lifespan with the electron holes before recombining again [36]. The semiconductors used as photocatalysts in the treatment of water and wastewater need several criteria. According to Lee et al. [37], when the mineralization process occurs, it does not create secondary pollution; it can be operated at room temperature, low pressure, inexpensive and continuously recyclable. The use of various pristine semiconductor nanomaterials as photocatalysts have been investigated extensively and their efficiency in various light sources for different wastewater contaminants are described in Table 1.

**Table 1.** List of metal oxides nanomaterials as photocatalyst and its efficiency towards various pollutants in wastewater.

Pollutants.	Catalyst	Method	% Removal	Band Gap (eV)	Time of Reaction (min)	Sources of Light	Ref.
Phenol, Methyl orange (MO) Rhodamine B (RhB)	$\text{TiO}_2$	Hydrolysis deposition and calcination crystallization	Phenol: 54, MO: 80.7, RhB: 84.2	3.05	Phenol: 360, Rh B and MO: 45	UV lamp	[38]
Tetracycline hydrochloride	$\text{TiO}_2$	Sol-gel (450 °C for 2 h)	18.2	3.17	120	30 W LED lamp	[39]
Ponceau BS	$\text{TiO}_2$	Sol-gel (450 °C for 4 h)	24.45	3.22	27	125 W mercury lamp	[40]
Methyl orange	$\text{TiO}_2$	Impregnation	42.98	-	60	150 W mercury lamp	[41]
Rh B	$\text{TiO}_2$	Solvothermal (180 °C for 24 h)	34.1	3.06	150	300 W Xe arc lamp	[42]
Methyl orange	$\text{TiO}_2$	Hydrothermal (180 °C for 18 h) and calcination (350 °C for 2 h)	4.6	3.10	60	500 W Xe lamp	[43]
Methyl orange	$\text{TiO}_2$	Polyol (500 °C for 2 h)	24	-	90	12 units of 100 W fluorescent lamps	[44]
Congo red	$\text{ZnO}$	Microwave-assisted hydrothermal	53.1	3.25	60	100 W UV lamp	[45]
Methyl orange	$\text{ZnO}$	Bio synthesis (450 °C)	83.99	3.32	120	8 W mercury lamp	[46]
Flumequine	$\text{ZnO}$	Chemical precipitation	11	3.24	240	UV lamp	[47]
Methylene blue	$\text{ZnO}$	Seed layer deposition and chemical bath deposition	54	3.32	240	Solar light	[48]

Table 1. Cont.

Pollutants.	Catalyst	Method	% Removal	Band Gap (eV)	Time of Reaction (min)	Sources of Light	Ref.
Phenol	ZnO	In situ preparation (hydrolysis)	56	-	240	40 W UVC lamp	[49]
Doxorubicin	BiFeO <sub>3</sub>	Thermal decomposition (480 °C for 1 h)	79	2.1	180	UV lamp	[50]
Tetracycline	BiFeO <sub>3</sub>	Sol-gel (550 °C for 2 h)	27.3	2.09	180	300 W Xe lamp	[51]
Methyl violet	Bi <sub>2</sub> Fe <sub>4</sub> O <sub>9</sub>	Hydrothermal (180 °C for 72 h)	10.6	-	180	Visible light	[52]
Rhodamine B	Bi <sub>25</sub> FeO <sub>40</sub>	Hydrothermal (180 °C)	62	1.8	240	500 W Mercury-Xenon lamps	[53]
Rhodamine B	Bi <sub>25</sub> FeO <sub>40</sub>	Hydrothermal (150 °C for 2 h)	28	2.78	180	240 W Xe lamp	[54]
Rhodamine B, BPA	BiFeO <sub>3</sub>	Co-precipitation	Rh B: 10, BPA: 7	2.16	Rh B: 60, BPA: 120	250 W Tungsten lamp (visible)	[55]
Methyl orange	MgO	Sonication assisted solvothermal (180 °C for 10 h)	43	-	120	90 W UVC lamp	[56]
Methylene blue	MgO	Biosynthesis ( <i>Ricinus communis</i> L.)	49.9	3.54	120	Solar light	[57]
Methylene blue	CuO	Thermal decomposition (350 °C for 2 h)	75	1.66	80	Solar light	[58]
Methyl orange, Methylene blue	CuO	Reflux condensation	MB: 93.66, MO: 95.63	1.29	MO: 120, MB: 180	UV lamp	[59]
Congo red	CuO	Co-precipitation	77	1.60	180	300 W Xe lamp	[60]
Sulfamethoxazole	WO <sub>3</sub>	Hydrothermal (140 °C for 8 h)	46.2	2.75	180	200 W Xe lamp	[61]
Rhodamine B	WO <sub>3</sub>	Hydrothermal (180 °C for 12 h)	14.7	2.46	140	300 W Xe lamp	[62]
Methylene blue	Al <sub>2</sub> O <sub>3</sub>	Sol-gel (600 °C for 8 h)	14	4.9	90	11 W UV lamp	[63]

### 2.1.1. Titanium Dioxide (TiO<sub>2</sub>)

The most common semiconductor in the field of photocatalysis is titanium dioxide or titania (TiO<sub>2</sub>). Depending on the bandgap, this material has three phases: anatase, rutile, and brookite [64] which is a nontoxic photocatalyst and has a fast response even in low light with excellent photo-efficiency [37]. Via different modes of synthesis, the properties of TiO<sub>2</sub> can be altered and subsequently affect its efficiency. Despite its widespread usage in the field of photocatalysis (Table 1), the downside is their large bandgap. It was only applicable under UV light in the bandgap range of 3.0–3.2 eV [37]. The use of energy would be low even when studying under direct sunlight, as the UV in the solar system only consists of 5 percent, thus impairing its effectiveness. Other than that, titania aggregation can occur during the experiment. The researcher's work, therefore, concentrated on improving the performance of titania, which will be further discussed in other sections.

### 2.1.2. Zinc Oxide (ZnO)

Zinc oxide (ZnO) has also been used in water treatment as a heterogeneous photocatalyst for semiconductors. It is unique because, in the UV spectral region, it has a direct and wide bandgap of 3.32 eV, great photocatalytic property, and good potential for oxidation [46]. ZnO exists in the white powder form, possesses hexagonal crystals, odorless, has a bitter taste, and is insoluble in water [65]. ZnO's bandgap is slightly similar to TiO<sub>2</sub>, making it more interesting and cheaper than titania in large-scale operations [66]. In addition, ZnO has strong antimicrobial properties; thus, it has a strong influence on the microflora in the environment. Compared to other metal oxides [67], ZnO is able to absorb a wide variety of solar spectrum and photons. Nonetheless, the drawbacks are photo-corrosion and involve tuning to generate material [65] with a narrow bandgap. Therefore, much

work has been carried out to improve water treatment efficiency by tuning the structure, morphology, and properties. In contrast, ZnO has recently been reported to have adverse effects on human and environmental conditions [68]. Monsé C and coworkers [69] reported that human exposure to ZnO nanoparticles would cause “zinc fever”. Symptoms such as throat pain, metallic taste, coughing, and flu have been reported. Thus, as an alternative to ZnO, an environmentally friendly photocatalyst may be considered.

### 2.1.3. Bismuth Ferrite ( $\text{BiFeO}_3$ )

Bismuth ferrite (BFO) is a semiconductor recently focused on photocatalysis as an alternative to titania and ZnO, especially in wastewater treatment. Some of its quality in the treatment of wastewater are indicated in Table 1. There are three structures of bismuth ferrite, the form of impurities called—sillenite ( $\text{Bi}_{25}\text{FeO}_{40}$ ) and mullite ( $\text{Bi}_2\text{Fe}_4\text{O}_9$ )—and the pure form—perovskite ( $\text{BiFeO}_3$ ) [22]. As stated by Li et al. [26], the BFO nanomaterial has exciting properties that make it a rising photocatalyst, with a narrow bandgap at approximately 2.4 eV. This feature allows BFO to be a visible light-active photocatalyst material with a wide spectrum of light absorption.

Moreover, it is a few materials that possess multiferroic properties at room temperature [70]. Multiferroic materials exhibit both ferroelectric and ferromagnetic properties in the same phase [71]. BFO shows ferroelectric characters with high Curie temperature ( $T_C$ ) of 830 °C and antiferromagnetic ordering with a Néel temperature ( $T_N$ ) of 370 °C [72]. The magnetic properties make the process of reusability much more convenient and preventing secondary pollution as the suspended BFO can be recover utilizing magnet. However, there is a drawback with the BFO; the recombination rate between the pairs of electron-hole is rapid, causing a reduction in the rate of photodegradation [52]. Therefore, modification of the pristine BFO improved the efficiency of photocatalytic degradation.

### 2.1.4. Other Metal Oxides

In wastewater treatment research, a few other metal oxides have been used, such as cupric oxide ( $\text{CuO}$ ) [58], magnesium oxide ( $\text{MgO}$ ) [73], aluminum oxide ( $\text{Al}_2\text{O}_3$ ) [74], and tungsten trioxide ( $\text{WO}_3$ ) [62].  $\text{CuO}$  is one of the transition metal oxides and a semiconductor of the p-type. In bulk form, it has a very narrow bandgap, which is 1.2 eV [75], and it draws the attention of researchers to work on it in photocatalytic application. The three significant phases obtained in  $\text{CuO}$  synthesis are monoclinic, cubic, and tetragonal. Among those three phases, the monoclinic phase is widely used in photocatalysis [76]. The downside of  $\text{CuO}$  is that it has a high recombination rate of electron holes, which causes the system to generate less reactive oxygen species and decreases the efficiency of photodegradation. In water treatment, magnesium oxide ( $\text{MgO}$ ) is another metal oxide since it benefits from adsorbing contaminants, mainly organic matter. This property increases the efficiency of removal because adsorption is one factor that efficiently occurs in wastewater treatment [73]. The bandgap reported by the previous study is approximately 5.51 eV [77] and varies according to the size of the particles. The wide  $\text{MgO}$  bandgap causes it to not be active under visible light irradiation, and researchers are drawn to reducing the bandgap.

In addition, aluminum oxide ( $\text{Al}_2\text{O}_3$ ) is a metal oxide used in water remediation as an adsorbent [78], catalyst support [79], and photocatalyst [74] due to its large surface area that adsorbs a large number of contaminants molecules. For  $\text{Al}_2\text{O}_3$ , there are many different crystal phases, known by  $\gamma$ ,  $\delta$ ,  $\theta$ ,  $\eta$ , and  $\alpha$ - $\text{Al}_2\text{O}_3$ .  $\alpha$  and  $\gamma$ - $\text{Al}_2\text{O}_3$  have the highest surface areas, so they have the most significant adsorption capacity [63]. Nonetheless, this material's bandgap is more than 3.0 eV, considered a wide bandgap, and not visible light active [63,74]. With some modifications to the alumina surface [80], this bandgap can be reduced to as low as 2.5 eV to ensure it can be a visible light-active material. Therefore, heterojunction with other materials and modification of alumina's surface has increased the photocatalytic activity and shortened the time it takes to cause degradation.

Lastly, the alternative photocatalyst used in wastewater treatment is tungsten oxide ( $\text{WO}_3$ ), an n-type semiconductor [81]. The crystal structure of  $\text{WO}_3$  is temperature-



dependent as it can be in triclinic ( $-50$ – $17$  °C), monoclinic ( $17$ – $330$  °C), orthorhombic ( $330$ – $740$  °C), and tetragonal structure ( $>740$  °C) [82]. As Weng et al. [81] and Cao et al. [62] reported, the bandgap of this metal oxide ranges from 2.4 eV to 2.8 eV. This narrow bandgap makes the material active, with more excellent absorption on most visible light regions in the solar spectrum.  $\text{WO}_3$  makes the photocatalyst a better alternative because it has excellent photo corrosion resistance, is nontoxic, and is physiochemically safe [61]. Nonetheless, due to the quick recombination rate of electron-hole pairs and slow charge transfer, the photocatalytic activity of the pristine  $\text{WO}_3$  is considered limited [61,62]. The electron-hole pairs' lifespan is influenced by this barrier, which later reduces the photodegradation of pollutant molecules. Hence, performance enhancement strategies such as interfacial and surface alteration, doping, heterojunction, and morphology control should be applied to render those drawbacks.

### 3. Reduced Graphene Oxide

Due to the remarkable properties of graphene, the discovery of graphene was initiated in 2004 by Geim and his colleagues [83]. It has high charge carrier mobility, unique transport efficiency, good mechanical properties, high thermal conductivity, and theoretically high surface area. Nevertheless, because of the strong van der Waals interactions and  $\pi$ - $\pi$  stacking between graphene sheets, graphene has low water dispersibility. It therefore, readily undergoes irreversible agglomeration to form graphite in an aqueous solution, limiting its applications. For this purpose, the incorporation of hydrophilic functional groups on graphene sheets through the oxidation of graphene or the reduction of graphene oxide (rGO) would eliminate the disadvantage of this carbon material. There are many rGO synthesis methods were reported elsewhere. Mechanical exfoliation was the first approach used and was performed multiple times to extract graphene film [83,84]. Later, four simple processes, such as Staudenmaier, Hofmann, Brodie, or Hummers [85], were used to produce graphene oxide (GO) prior chemically reduced into rGO. Most of these approaches have the ability to enhance and produce positive performance with simple and cost-effective methods. The effectiveness of an oxidation method is also determined by the graphene oxide's carbon/oxygen ratios. Hummer's method is the most promising technique of rGO produced, as shown in Figure 1.

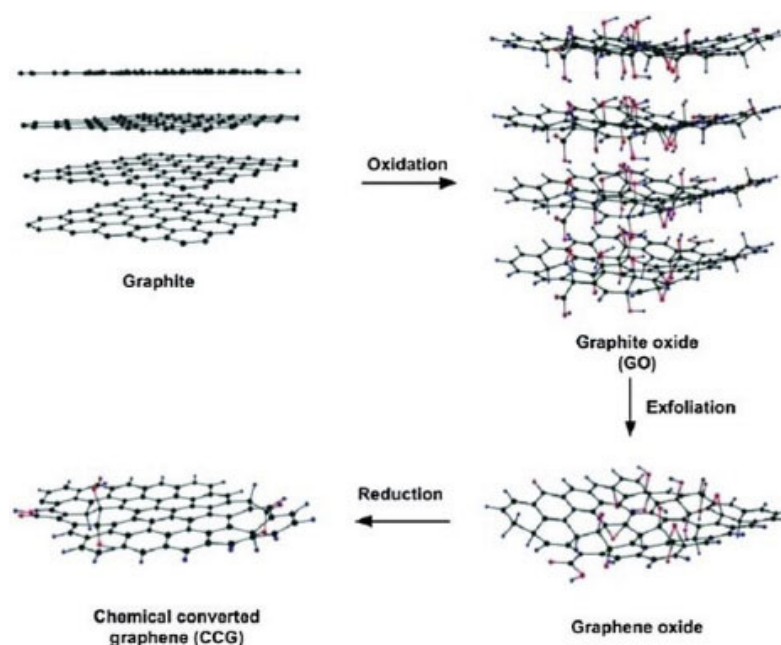


**Figure 1.** Preparation of graphene by chemical reduction of graphene oxide synthesized by Hummers' method. Reproduced with the permission from [84].

In particular, graphene [86] is a single hexagonal two-dimensional layer and is structured in a carbon atom  $sp^2$ -bonded layer. In addition, the three  $sp^2$  hybrid orbitals dominate a graphene layer, which will bond with carbon atoms and leave the fourth bond to be a dangling bond perpendicular to the hexagonal array of carbon atoms. Any functional groups in the solution or another graphene sheet can be attached to this dangling bond. A single layer of graphene sheet can be peeled off from the 3-dimensional graphite by mechanical or chemical means. Once the graphene is peeled off and deposited in a liquid solvent, some of the functional groups contained in the solvent will cover the sheets. It is oxidized into graphene oxide (GO) if the graphene is immersed in the solvent. The epoxide, carboxyl, and hydroxyl functional groups have covered the surface of the GO. In addition, by adding hydrazine hydrate, sodium borohydride and other reducing agents to the GO solution or modifying the synthesis conditions, the graphene oxide can be reduced to become reduced graphene oxide (rGO). From this approach, only the hydroxyl functional groups will cover the surfaces of the rGO.

The benefits of rGO are that it has specific characteristics that have made it appealing, such as high conductivity, large specific surface area, strong ability to adsorb, and optical clarity [87]. The lack of an extended  $\pi$ -conjugated orbital carbon in GO causes low electrical conductivity of that material compared to rGO [22]. Besides, due to the reduction process, rGO does not have some absorption peaks that appear in GO, especially the functional group peaks containing oxygen [87]. Due to the growth of the  $sp^2$  domain [87], the ratio of D band to G band for rGO is higher than that of GO in Raman spectroscopy. The potential applications in the areas of batteries [88], supercapacitor [89], electrode [90], and catalyst [27] have been used with the incorporation of rGO in those multifunctional materials. The presence of such nanomaterials on the graphene surface is highly desirable for the tuning surface. The morphology, electronic structure, and graphene's intrinsic properties make it a valuable candidate for photocatalytic activity enhancement.

### 3.1. Hybridization of rGO within Semiconductor Nanomaterials

A poor performance against photocatalytic degradation of organic contaminants in wastewater utilizing most pristine materials has been shown and recorded in Table 1. The existing photocatalysts have many limitations; for example, the need for UV light response photocatalysts involves costly setup and an agglomeration of nanomaterials, which reduced the material surface area and consequently decreased the efficiency of photocatalytic operation [27]. The perovskite material, i.e.,  $BiFeO_3$ , effectively has a narrow bandgap facing a rapid recombination rate obstacle and consequently decreases its effectiveness in photodegradation [36]. A critical strategy to overcome these challenges has been introduced with the emergence of nanotechnology and advanced materials. Recently, a semiconductor nanomaterials hybridization strategy with graphene and its derivative, particularly rGO, reduced graphene oxide, has attracted considerable attention [91–95]. Composites based rGO provide the superior photocatalytic ability and efficient photodegradation of a wide variety of organic pollutants. These modifications causing the bandgap of pristine photocatalyst's being narrower and active in visible light. Other than that, the improvement helps to reduce the recombination rate.

The composite based rGO will serves as an effective electron acceptor, improving photoinduced charge transfer, hindering charge carrier recombination, and increasing photocatalytic activity due to the remarkable characteristics of rGO, as mentioned earlier. In addition, rGO integration subsequently reduces agglomeration and increases the surface area of the composites. In addition, with high active sites exposed within the composites, rGO can serve as nucleation sites for the photocatalysts to develop in a well-dispersed manner, which later improves photocatalytic degradation efficiency. Furthermore, the composites' specific surface area increases by adding rGO to the semiconductor photocatalysts, which allows electron mobility on the surface of the catalysts and decreasing the rate of electron-hole pair recombination. The rGO functional groups will interact by  $\pi$ - $\pi$  bonding

with the contaminants' structure, resulting in the synergistic effect of photocatalysts with good adsorption properties [96].

### 3.1.1. Strategies and Performance of Hybridization rGO-Based Photocatalyst

The hybridization of photocatalysts with electron acceptor materials such as rGO is one of the commonly used strategies to enhance the photocatalytic behavior of photocatalysts. Li et al. [97] deduced a strategy of hybridization, as simplified in Figure 2, of the energy levels of C2p and O2p. For instance, in rGO and TiO<sub>2</sub> or SiO<sub>2</sub> composites, the creation of a new valence band is induced, which would consequently minimize the composite bandgap.

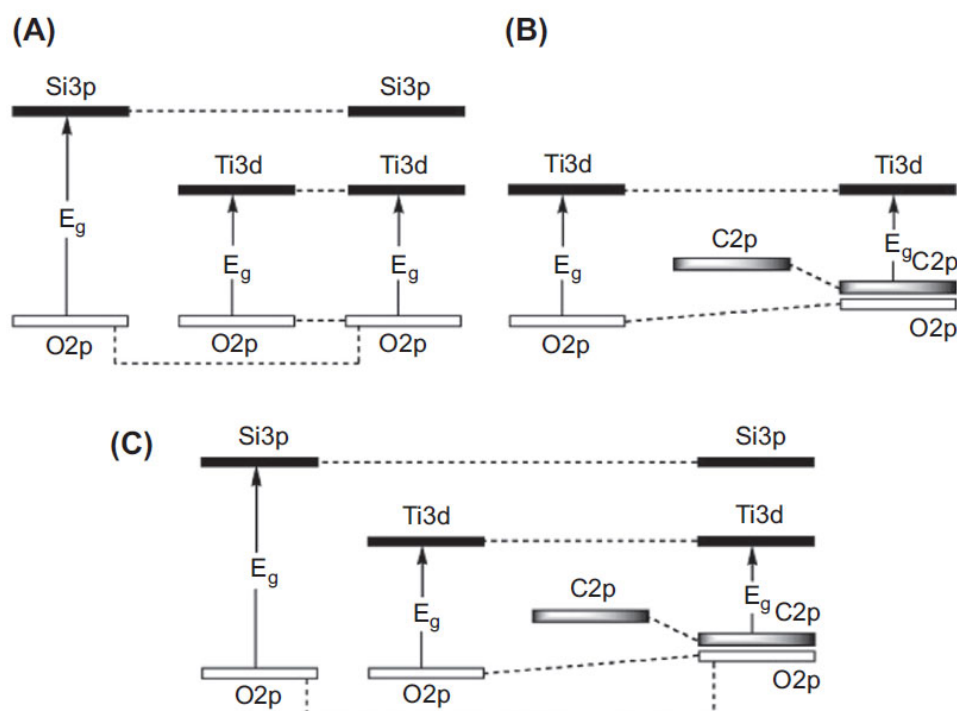


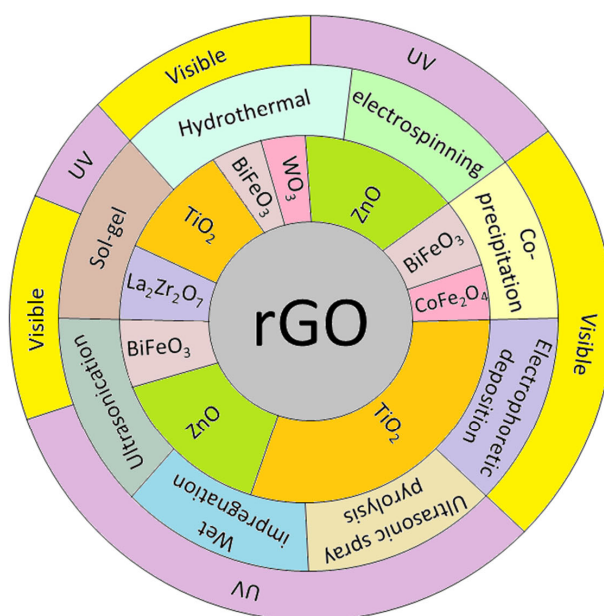
**Figure 2.** Simplified representation of hybridization of C2p and O2p orbitals and the formation of new valence bands, which reduce the bandgap. (A) TiO<sub>2</sub>/SiO<sub>2</sub>, (B) graphene-based NeTiO<sub>2</sub>, and (C) graphene-based NeTiO<sub>2</sub>/SiO<sub>2</sub> composites. Figure use with permission from [97].

Researchers have prioritized the production of advanced composite materials involving two or more semiconductors to boost the efficiency of the photocatalyst [22,26,87,91–93,98–109]. These multicomponent semiconductors lead to improvements in photocatalytic properties, reusability, and photostability due to improved charge separation and the great ability to absorb visible light. Some of the photocatalyst materials synthesized in the binary and ternary composites systems described in Table 2 and Figure 3 improved photocatalytic degradation due to the efficient transport of photoinduced electrons from the conduction band to the rGO sheets in different light sources. In addition, rGO nanosheets have a high specific surface area, and these sheets can prevent the agglomeration of nanoparticles from semiconductors and help them diffuse on the rGO and disperse well. Such particles have an excellent ratio of surface to volume and can serve as active centers. rGO also prevents the semiconductor nanoparticles from photo corrosion and affects their crystal structure, impacting their photocatalytic activity later.



**Table 2.** Hybridization of various metal oxides with reduced graphene oxide (rGO) using different methods.

Pollutants.	Catalyst	Method	Optimum Concentration of rGO/GO	% Removal	Band Gap (eV)	Time of Reaction (min)	Sources of Light	Ref.
Methylene Blue	BiFeO <sub>3</sub> /rGO	Hydrothermal (160 °C for 6 h)	3 mg/mL	92	2.4	140	150 W Xe lamp	[26]
Chromium (VI)	rGO-TiO <sub>2</sub> -ZnO	Hydrothermal (180 °C for 20 h)	0.5 mg/mL	63	-	120	100 W Mercury lamp	[87]
Methylene blue, Reactive black 5	Ag-ZnO/rGO	Hydrothermal (140 °C for 2 h)	10 mg	MB: 61, RB5: 85	-	200	Mercury-vapor lamp	[91]
Tetracycline, Chlortetracycline, Oxytetracycline, Doxycycline	BiVO <sub>4</sub> /TiO <sub>2</sub> /rGO	Hydrothermal (200 °C for 6 h)	0.5%	TC: 96, OTC: 98, CTC: 96, DC: 100	2.29	120	1000 W Xenon lamp	[92]
Methylene blue	WO <sub>3</sub> /rGO	Hydrothermal (120 °C for 24 h)	0.2%	98	2.7	360	300 W Xe lamp	[93]
Tetracycline	La <sub>2</sub> Zr <sub>2</sub> O <sub>7</sub> /rGO	Sol gel	0.5 g	82.1	2.42	40	300 W Xe lamp	[98]
Eosin blue	Zr-TiO <sub>2</sub> /rGO	Sol-gel (70 °C for 24 h)	5%	96	2.95	90	400 W mercury vapour lamp	[99]
Bisphenol A (BPA)	BiFeO <sub>3</sub> /rGO	Ultrasonic (40 kHz, 10 min, 40 °C)	4%	98	1.9–2.0	70	55 W Fluorescent lamps	[100]
Methylene blue, Acid red 249	ZnO/rGO	Ultrasonic (40 kHz, 1 h, 500 W)	2%	MB: 92.9, AR249: 94.8	-	120	15 W UV lamp	[101]
Methyl orange	Cu-TiO <sub>2</sub> /rGO	Wet impregnation	2%	99	3.08	90	UV lamp	[102]
Methylene blue	ZnO/rGO	Wet impregnation	0.5 g	94	3.17	45	125 W UV lamp	[103]
Bisphenol A (BPA)	Bi <sub>2</sub> Fe <sub>4</sub> O <sub>9</sub> /rGO	Co-precipitation (95 °C)	4.5%	80	2.3	180	150 W Xe arc lamp	[22]
Methyl orange, Rhodamine B, Methylene blue	CoFe <sub>2</sub> O <sub>4</sub> /rGO	Co-precipitation (160 °C)	25%	All dyes: 100	0.85	MO: 60, MB: 75, Rh B: 45	100 W reading lamp	[104]
Chromium (VI)	rGO/TiO <sub>2</sub>	Electrophoretic	0.1 mg/mL	100	-	60	Solar simulator	[105]
Methylene blue	rGO/TiO <sub>2</sub>	Electrophoretic	0.8 g/L	19	-	30	UV light	[107]
Methyl orange	ZnO/rGO	Electrospinning	0.2%	99	-	360	220 W UVA lamp	[108]
Methylene blue	rGO/TiO <sub>2</sub>	Ultrasonic spray pyrolysis	5%	UVA: 40.8 UVC: 100	2.72	UVA: 15 UVC: 60	UVA or UVC lamp	[109]

**Figure 3.** Illustration of various composites of rGO/semiconductors with their method of hybridization and suitable light energy represented from Table 2.

In addition, the existence of rGO, as Prabhu et al. [110] stated in their work on ZnO/rGO nanocomposites, helps to shift the bandgap of UV light active to solar light active semiconductors. Sharma and Lee [111] reported adding NiO to TiO<sub>2</sub>/rGO, resulting in a bathochromic change in the composite bandgap due to the interaction of Ti<sup>4+</sup> and Ni<sup>2+</sup> in the 3d level conduction band. In addition, rGO considered as an electron sink, which enhancing the photocatalytic activity of the composite and subsequently reduce the recombination rate of the photo-induced electron-hole pairs [112].

Several strategies, such as hydrothermal [26], ultrasonic [100], co-precipitation [22], electrophoretic [105], sol-gel [98], reflux column [113], electrospinning [108], ultrasonic spray pyrolysis [109], and wet impregnation [102], can be used to integrate rGO into semiconductor photocatalysts. Some of the strategies are mentioned in Table 2 and addressed in the next subsection. In order to generate optimal photocatalysts, each technique has its parameters, such as temperature and time, to be considered. Variation of the nanocomposite morphologies observed with various integration strategies of semiconductors in the presence of rGO as depicted in Figure 4. It is crucial to note that the different morphologies produced by different techniques [27,95,98,103,105,108,109,114] will alter the bandgaps and other characteristics and lead to its performance reliability.

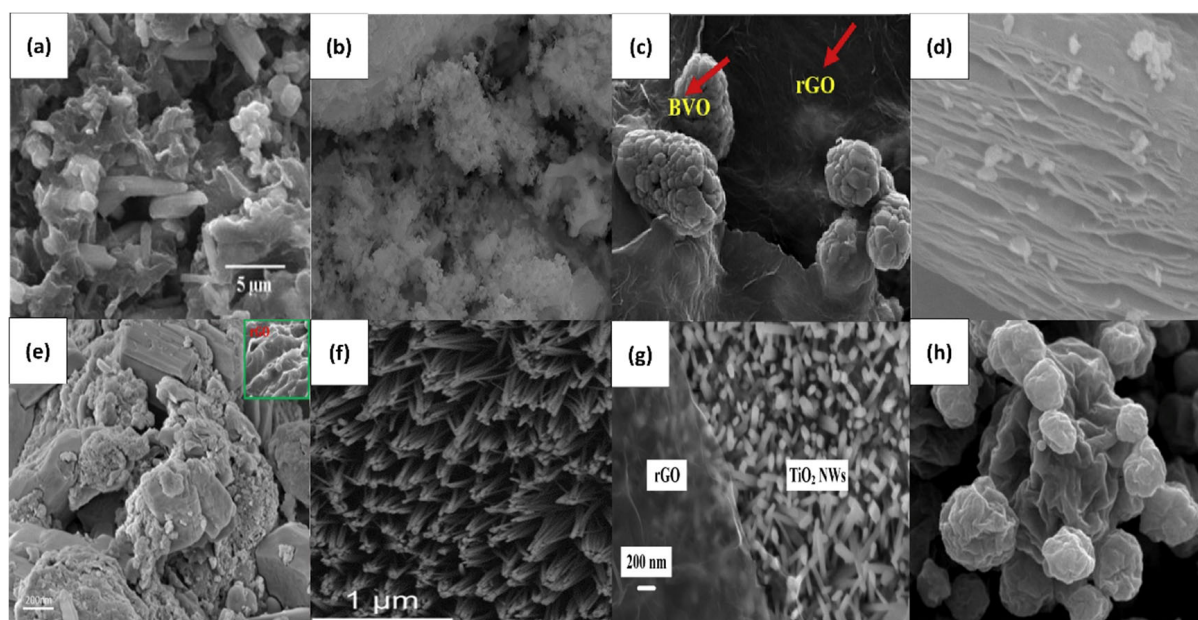


**Figure 4.** Variation of the nanocomposite morphologies observed with various integration strategies of semiconductors in the presence of rGO: (a) hydrothermal (ZnO/rGO), (b) sol-gel (La<sub>2</sub>Zr<sub>2</sub>O<sub>7</sub>/rGO), (c) ultrasonication (BiVO<sub>4</sub>/rGO), (d) wet-impregnation (rGO/ZnO), (e) co-precipitation (rGO-TiO<sub>2</sub>/Co<sub>3</sub>O<sub>4</sub>), (f) electrospinning (ZnO/rGO), (g) electrophoretic deposition (rGO/TiO<sub>2</sub>), and (h) spray pyrolysis (rGO/TiO<sub>2</sub>). The figure is reproduced with permission from [27,95,98,103,105,108,109,114].

### Hydrothermal Method

There was extensive synthesis of nanomaterials and integration with rGO using the hydrothermal process. The hydrothermal method refers to the synthesis of materials above ambient temperature and pressure in a closed system and heated solution. [115]. The hydrothermal device consists of two elements, typically made up of a Teflon-lined container [116], a polyphenylene polymer (PPL)-lined container, or a thick-walled glass [117] that was used in the first hydrothermal synthesis. Different materials have different temperatures and pressures in the internal part to ensure the process's sustainability. These containers are slotted into the autoclave of stainless steel that is the outer component without any space between them. The hydrothermal method used to integrate semiconductor nanomaterials with rGO was recorded in enormous research studies, such as

rGO/TiO<sub>2</sub> [118–122], rGO/ZnO [95,123], rGO/WO<sub>3</sub> [61], and rGO/BFO [26,51,71,124]. The benefits of the hydrothermal process are that the operating environment is moderate, which includes low temperatures below 300 °C; eco-friendly; inexpensive and has good dispersion with one-step procedure [115].

The use of the hydrothermal process in the synthesis of rGO/TiO<sub>2</sub> was reported by Ruidiaz-Martínez et al. [118]. The solvents used in the synthesis steps are water and ethanol, and the precursor mixture was subjected to heat at 180 °C for 24 h after being combined and ultrasonicated in a 120 mL stainless steel Teflon-line autoclave reactor. After the heat treatment, the product was washed and dried in order to obtain the desired product. The photodegradation performance towards ethylparaben between optimal rGO composite and pristine titanium under UV light has been compared and the efficiency found was 98.6 and 72.5%, respectively. An increase in the composite's photocatalytic efficiency can be observed due to the reduction in the composite's bandgap from 3.20 eV to 2.75 eV. Wang et al. [119] have also synthesized rGO/TiO<sub>2</sub> in a 100 mL vessel using a similar method with a heating temperature of 150 °C for 5 h. The morphology of the product is a spherical agglomerate structure for both pristine and composite. The photocatalytic efficiency is 23% higher than commercial Titania for the optimum composite. As the amount of rGO in Titania is higher than the optimum, the efficiency was observed to be reduced due to light scattering of the composite that prevents UV light absorption.

In other research studies by Khamboonrueang et al. [125], they reported the efficiency of titanium dioxide decorated reduced graphene oxide nanocomposite via the hydrothermal process to eliminate inorganic contaminants. To minimize the inorganic compound of Cr<sup>6+</sup> ions to nontoxic Cr<sup>3+</sup> ions, they investigated the use of TiO<sub>2</sub> x% rGO nanocomposites (x = 1, 5, 10, 15, 20, 25). The results found that, with the increase in rGO content, the photocatalytic for reduction in the toxic Cr<sup>6+</sup> increased, as shown in Figure 5a. In addition, Srirattanapibul et al. [126] reported that ZnO decorated the reduced graphene oxide (rGO) nanocomposites on the photocatalytic reduction of Cr<sup>6+</sup>. They showed that the photocatalytic reduction of the toxic Cr<sup>6+</sup> was observed by the time change in the absorption of light at two wavelengths 273 nm and 373 nm (Figure 5b and c). The enhancement in the photoreduction rate increased, reaching a maximum at x = 10%. Han [127] investigated the performance Cu<sub>2</sub>O-rGO nanocomposites on the photodegradation of methylene blue under visible light. The results showed an increase in photocatalytic activity of the Cu<sub>2</sub>O-rGO nanocomposites. The nanocomposites' enhancement comes from the extended range of the light absorption and the transfer of photogenerated electrons of Cu<sub>2</sub>O to rGO, obtained easier with better charge separation, corroborated by photoluminescence. Zhigang [128] and Sun [129] also reported the intense enhanced photocatalytic activity of Cu<sub>2</sub>O and rGO nanosheets on rhodamine B degradation. Zou [130] synthesized Cu<sub>2</sub>O-rGO composites for methylene blue degradation under visible light. He found that the photocatalytic activity of the composites influenced by the Cu<sub>2</sub>O crystal facet and that the (111) facet showed the enhanced visible light absorption and faster charge-transfer rate. It can be related to interfacial interactions and electronic structures.

In producing rGO/ZnO hybrid nanocomposites, another hydrothermal method reported by Dong et al. [95] was applied. Preparation began with sonication of the precursor mixture, followed by stirring and addition of mineralizer, then adding the reduction agent for 10 h before heating at 180 °C, and drying overnight. The pristine ZnO has a rod-like structure, and the inclusion of rGO exhibited ZnO nanoclusters well-decorated with carbon content. The ZnO nanocluster was intercalated into rGO sheets and formed a sandwich-like structure. The use of synthesized composite and pristine ZnO in metronidazole degradation was measured, and the results obtained were 49.3 and 16.9%, respectively, after 160 min irradiation. The existence of rGO resulted in an increased surface area of nanomaterials, increased light absorption efficiency, and decreased recombination rate of charge. Other than that, using the comparable form, rGO/WO<sub>3</sub> was also synthesized [93] within 8 h in 45 mL deionized water. The temperature used in this synthesis was 140 °C. The composite rGO/WO<sub>3</sub> exhibits a cube-like structure on the rGO sheet that reflects the WO<sub>3</sub>

nanoparticles with an average size of 150–200 nm. The aggregation of  $\text{WO}_3$  nanoparticles was prevented, and the photocatalytic degradation of sulfamethoxazole was thus increased. In comparison to pristine  $\text{WO}_3$ , the optimal rGO/ $\text{WO}_3$  composite (98%) resulted in higher degradation efficiency as compared to unmodified with only 46.2%. In the presence of rGO in the system, the bandgap of the pristine  $\text{WO}_3$  was successfully reduced from 2.75 eV to 2.15 eV.

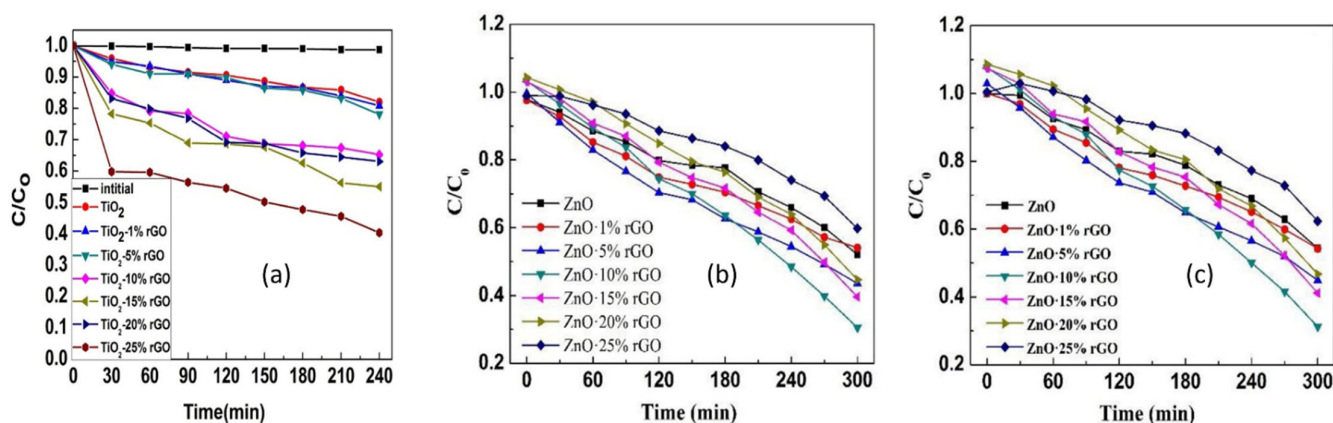


**Figure 5.** (a) The absorption peaks at 255 nm and 349 nm are due to the absorption by the  $\text{Cr}^{6+}$  ions in the presence of x% rGO nanocomposites NCs. Photocatalytic reduction of  $\text{Cr}^{6+}$  by  $\text{ZnO}$ -x% rGO NCs deduced at the wave length of (b) 273 and (c) 373 nm from absorbance of the light. The figure is reproduced with the permission from [125,126].

Finally, the production of  $\text{BiFeO}_3$  in the presence of rGO through the hydrothermal method and its efficiency against methylene blue [51] was observed. The method of preparation was almost the same as stated earlier except that the heat treatment was 180 °C for 24 h and the mixture of nitric acid and potassium hydroxide solution was in the 50 mL Teflon vessel. The composites of rGO/BFO obtained formed a rougher surface of the spherical structure compared to pure BFO. As the rGO network that exists in the system limits the growth of BFO nanoparticles, the particle size of BFO in the composite is smaller than pure BFO. rGO/BFO shows an excellent photodegradation efficiency of methylene blue compared to pure BFO, with the percentage removal at 92% and 34%, respectively. The incorporation of rGO imparts the disadvantages of the rapid electron-hole pair recombination rate of BFO. With different Teflon vessel lengths, heating temperatures, and time, the hydrothermal approach has been commonly used as these significant parameters can be easily altered to achieve the desired morphology and nanomaterial crystallinity for effective performance.

### Sol-gel Method

Sol-gel can be defined as a method that suspends the solid particles in a solvent that forms the “sol”. The particles are polymerized to form a “gel” by the addition of an initiator and evaporation of the solvent. The process begins with heating at a high temperature, typically to give the final product in a powder form via calcination. The surface area, pore size distribution, texture stability, homogeneity, and structural properties that can affect the purity of the catalyst and the composition of the product can be regulated by the sol-gel process [131]. This is another technique for semiconductor nanomaterials synthesis with rGO. A one-step sol-gel method was used for simultaneous development of the  $\text{La}_2\text{Zr}_2\text{O}_7/\text{rGO}$  (LZO/rGO) composite and GO reduction, according to Wang et al. [98]. The preparation begins with the precursor and ethylene glycol being mixed prior to changing the pH to form collosol. Collosol was then dried for 6 h in the oven at 125 °C before being subjected to 800 °C for 1 h. The morphology of the composite can be clearly seen under a scanning electron microscope (SEM) by the aggregation of pristine LZO distributed in blocks, while spherical distribution on the rGO sheet can be observed for the optimal LZO/rGO composite. It has been shown that the aggregation of pristine particles



can be reduced by the presence of rGO. From the UV-DRS results, a slight reduction in the bandgap can be observed, where the measured band gaps for pristine LZO and LZO/rGO are 2.56 and 2.42 eV, respectively. This helps to improve the range and efficacy of light absorption by the composite. Utilizing the optimal composite, the overall degradation of tetracycline is 82.1% compared to the pristine LZO with only 57.8%. Increases in efficiency are due to the incorporation of rGO, which decreases the recombination rate of electron-hole pairs and provides a greater adsorption surface region.

Next, as Banerjee et al. [132] reported, using the simple sol-gel process, the fabrication of rGO-TiO<sub>2</sub>-Fe<sub>3</sub>O<sub>4</sub> was achieved. Before being subjected to heat at 180 °C for 10 h, each part of the precursor was combined, stirred, and sonicated. The morphology of the obtained composite has a platelet-like structure, where the metal oxide particles are attached to the surface of the rGO, and increasing rGO amounts do not affect the morphology of the composites. Moreover, the nanoparticles formed to prevent the agglomeration of the rGO sheets. The maximum photocatalytic degradation reached by the optimal composite against methylene blue is 94% in 9 min under visible light and 99% within 6 min under UV light. Semiconductor integration on the rGO sheets with the sol gel method was successful in producing stable morphologies of nanoparticles with high composite purity on rGO sheets.

#### Ultrasonication Method

Ultrasound requires the use of sound energy greater than 20 kHz (ultrasonic waves) in the liquid sample to agitate the particle in the sample. Then, a process called cavitation produces diffused sound energy in the cavity. When the liquid floods in and the cavity collapse, the tiny bubbles proliferate and can no longer absorb energy effectively. The collapsed and exploded bubbles release high energy, increasing the pressure and temperature that cool down the liquid later. These conditions provide an environment for turbulence synthesis and are ideal for a chemical reaction involving high energy. It is much easier to decompose organic and inorganic materials on a small core [133].

The method was used by Soltani et al. [100] to develop BiFeO<sub>3</sub>/rGO to degrade Bisphenol A (BPA). The preparation method was simple as it began to disperse the precursor materials in absolute ethanol, then subjected to ultrasonication at 40 °C for 10 min. The system continues with the drying process until the product formed. Sphere-like shapes of the BFO aggregate were found distributed in the composite on the rGO sheets. The implementation of rGO, reduced the BFO particle size and allowed BFO to be distributed homogeneously throughout the carbon sheets. There is a slight reduction in the bandgap of the pristine BFO (2.1 eV) when it is hybridized with rGO, based on the UV DRS results (1.9 eV). For pristine BFO and rGO/BFO, respectively, the overall photodegradation efficiency of BPA rises from 78% to 98%. With the introduction of rGO, the composite's adsorption potential is improved to help adsorb more pollutants that need to be degraded.

rGO/TiO<sub>2</sub> synthesis was also carried out using the ultrasonic or sonochemical method by Deshmukh et al. [134]. The ultrasonic method was performed for just 35 min in isopropanol solution. The distribution of TiO<sub>2</sub> on the rGO sheet was evenly dispersed based on the elemental map images and transmission electron microscopy (TEM). In the presence of rGO/BFO under alkaline conditions, the maximum degradation of methylene blue is 91.3% within 30 min, which exhibits high photocatalytic degradation efficiency.

Finally, to synthesize the heterojunction BiVO<sub>4</sub>/rGO (BVO/rGO) for tetracycline degradation, the ultrasonication procedure was used by Soltani et al. [27]. The visible-light-assisted photocatalytic reduction of graphene oxide was used for this synthesis. The precursor mixture was dispersed in an ethanol solution, ultrasonically irradiated at 30 °C for 30 min, and proceeded with visible light illumination and drying to create the BVO/rGO. The morphology of the BVO/rGO is a bundled dumbbell-like structure and smaller than the pure BVO. The incorporation of rGO to BVO has an impact on the nucleation and growth process of BVO on rGO sheets, thus enhancing the adhesion and dispersion of BVO on sheets, limiting restacking of rGO, and thus reducing the agglomeration of nanoparticles



of BVO [86]. The incorporation of rGO into the BVO decreases the bandgap from 2.30 eV to 2.21 eV and consequently increases the capacity to absorb light, leading to an improvement in photocatalytic efficiency. The maximum degradation that pure BVO can achieve under the same conditions that were optimized by Soltani et al. under 85 min is 85% whereas, for BVO/rGO, achieved 92%, and the time taken for complete degradation of tetracycline can be obtained using the composite by increasing the pH to 10.5. The ultrasonic method is an excellent synthesis method as it only requires short time and low-temperature conditions to integrate semiconductor nanomaterials into rGO.

#### Wet Impregnation and Co-Precipitation Method

Wet impregnation or incipient wetness impregnation is a heterogeneous catalyst synthesis technique and can be used to incorporate semiconductor nanomaterial on the surfaces of the rGO. The procedure takes place where the support is soaked for a particular time with the excess precursor solution, and then, the solid separation was conducted, and the drying process proceeded to eliminate excess solvent. The diffusion mechanism involves the transport of the solution into the pores in this process [135]. The parameters necessary to be managed in the synthesis are semiconductor particles' size, accessibility, and distribution over the support. This technique gained the researchers' interest [136,137] to produce a simple synthesis, cheaper choice, and low amounts of waste. This process, however, has challenges in synthesizing higher concentration catalysts and generating good catalyst dispersion on the support surface [135]. The composite reproducibility issue may be caused by these limitations and may affect the composites' efficiency and reusability.

The preparation of CuO-TiO<sub>2</sub>/rGO by Babu et al. [138] is an example of synthesis using wet impregnation. In order to improve the efficiency of impregnation, TiO<sub>2</sub> loaded on GO was dispersed in some concentrations of copper (II) nitrate solution and ultrasonicate. Later, the drying and calcination process continued for 5 h at 350 °C. The presence of tiny secondary particles (CuO) on the surface of the spherical structure (TiO<sub>2</sub>) on rGO surfaces could be deduced from the observation of its morphology. Within 120 min, the overall degradation of methyl orange by the optimal composite is 89%. This result shows that the existence of rGO helps to improve the efficiency of degradation by lowering the recombination rate and induce light absorption.

Co-precipitation is a method of simultaneous precipitation of more than one material from the solution and is typically regulated by pH change, metal salt concentration, and evaporation rate. These parameters help to adjust the catalyst's aggregation and growth of the crystal. Simple steps were needed and can be used to prepare support and bulk catalysts. In the precipitation process, there are three steps involved: supersaturation, followed by nucleation and growth. Precipitation may occur when there is interference in the supersaturation region, leading to the formation of small and stable particles known as nucleation. Then, under supersaturation conditions, the rate of nucleation is faster than the rate of crystal growth, and therefore, the particles produced are small and numerous. Those tiny particles continue to grow into the desired products [135]. The homogeneity depends on the kinetics of precipitation and the variations between the components' solubility. Heterogeneous products are likely to form if the precipitation rate is slow and the stirring speed is low, whereas good mixing can produce a homogenous product. Sequential precipitation can occur if one of the components is more soluble than the others, which leads to poor mixing of the components [139]. This approach could include post-treatment treatments such as filtration, drying, and calcination. This method has several drawbacks, such as the uneven particle size produced, incomplete metal ion precipitation, and agglomeration [135]. As the morphology and surface area are positively linked to their photodegradation behavior, these issues may impact the photocatalysts performance.

Hu et al. [22] utilized the facile co-precipitation method to produce rGO/Bi<sub>2</sub>Fe<sub>4</sub>O<sub>9</sub> for the degradation of BPA under solar irradiation. The preparation began with the ultrasonication of GO and Bi/Fe precursor solution, followed by the heat treatment at 95 °C and aging for 36 h. The final product was collected, washed, and dried. Bi<sub>2</sub>Fe<sub>4</sub>O<sub>9</sub> was successfully de-

posited on the surface of rGO in monodispersed particles with a size range between 4 and 5 nm, and good crystallinity. BPA is a recalcitrant chemical and hardly degrades, but both the composite and pristine BFO can degrade it up to 62% and 33%, respectively, within 3 h. Both methods prove that incorporating semiconductor nanoparticles into the rGO surfaces was successfully carried out under several parameters, including pH adjustment, solubility, and temperature. These parameters cause the degradation efficiency to be enhanced as rGO increases the surface area or adsorption and reduces the recombination rate.

#### Electrophoretic Deposition, Electrospinning and Ultrasonic Spray Analysis Methods

Electrophoretic deposition (EPD) is a method of depositing charged particles in a stable colloid in the presence of current flow that can be either direct current or alternating current on a conductive substrate [140]. The applications are wide-ranging since EPD requires only simple equipment, cost-effectiveness, short processing time, and easy modification to control the products' morphology and thickness. The deposition can be flexibly performed on different shapes, including cylindrical and flat surfaces [141]. EPD is a two-step mechanism where the migration of particles to the substrate begins in the presence of the electric field. Next, complex electrochemical reactions and aggregation were performed, and the deposited layer formed [140]. However, the disadvantage of this process is that it does not use water as the medium because the use of water voltage will generate hydrogen and oxygen gases that will later adversely affect the quality of deposits produced [141].

This process has been carried out in a laboratory scale by Rahmat et al. [105] to synthesize the composite of rGO/TiO<sub>2</sub>. The oxidized Ti foil and Pt rod were used as the anode and cathode, respectively. In the synthesis, direct current was applied, and the rGO solution was used as the electrolyte. The substance produced was used to degrade the heavy metal ion chromium (VI), and the efficiency was remarkable because, under visible light, it can completely degrade the pollutant in just 60 min. This approach was also used to prepare the rGO/TiO<sub>2</sub> nanocomposites by Noormohammadi et al. [107], and there are many improvements in the setup as Cu foils and graphite have been used as substrates and counter electrodes, respectively. The degradation of methylene blue was studied in their work, and the efficiency is 12 percent greater than the pristine TiO<sub>2</sub> removal. This shows that rGO can be hybridized with metal oxides using the EPD method and that the composite output is better than that of pristine metal oxide.

Electrospinning is a technique used to create fibers with sizes varying from micro- to nanometers in an untangled network. The system requires high voltage current used in the liquid solution, and the collector collects liquid jet production. This jet is later dried and deposited, contributing to fiber formation [142]. The distinction between electrospinning and electrospraying is that the electrospinning jet is in the continuous form of generating fibers instead of breaking into tiny droplets that can allow the electrospraying phase of particles to form. The electrospinning method can generally be performed in 4 stages, beginning with the electrical charge being added to the liquid droplet creating a cone-shaped jet; then the creation of the charged jet in a straight line; next, in the presence of an electric field and whipping turbulence, the procedure continues with the thinning of the jet; and with the gathering of the solidified jet in the form of fibers, the completion of this technique is achieved.

The benefits of this approach are that it is a flexible and easy way of synthesizing micro and nanofibers, and it is possible to monitor the morphology of the fibers [143]. The ZnO/rGO was synthesized successfully by Ramos et al. [108] using the electrospinning technique. The optimal voltages used in the experiment are 20, 30, and 40 kV. The syringe needle diameter is 0.6 mm, the length of the deposition is 3 h, and the sample has been calcined at 400 °C. The degradation of methyl orange achieved using the ZnO/rGO fibers is 99% at 6 h and better than that of the pristine sample (77% at 7 h). This work proved that the electrospinning method can hybridize rGO with semiconductor materials and enhance their photocatalytic activity.

Ultrasonic spray pyrolysis is a pyrolysis technique using ultrasonic atomizers to create droplets from the precursor solution [144]. It is a continuous spray technique carried out at ambient pressure, and the product is formed usually in the form of powder or film [145]. This method has been used to make ceramics powder, single and multi-layered film, and other materials powder because of its cost-effectiveness, versatility, simplicity, operation in an open chamber, continuous process, and high deposition rate [146]. Nevertheless, the limitation with the ultrasonic spray pyrolysis is that it has low output. This technique was carried out by several steps, which begin with the creation of droplets from a precursor solution, and later, the evaporation process takes place where the size of the droplets starts to decrease. Then, this precursor is converted into its oxides prior the formation of solid particles occurs [145].

Park et al. [109] performed the preparation of rGO/TiO<sub>2</sub> composites using ultrasonic spray pyrolysis. At the resonant frequency of 1.7 MHz, the precursor solution was sprayed, the flow rate of nitrogen carrier gas used was 5 L/min, and the temperature used to dry the sample was maintained at 600 °C. In this experiment, the synthesized rGO/TiO<sub>2</sub> composite was used to degrade methylene blue under UVC light and the efficiency of photodegradation obtained was 100% in 60 min. The composite performance was outstanding, and it could be due to the bandgap that decreased from 3.04 eV to 2.72 eV compared to bare TiO<sub>2</sub>. This illustrates that more light and visible light can be absorbed by rGO/TiO<sub>2</sub>. By using ultrasonic spray pyrolysis, the integration of rGO with metal oxides was achieved, and the composites show excellent efficiency in the treatment of wastewater.

#### 4. Mechanism of Photocatalytic Degradation of Organic Pollutants by rGO-Based Nanocomposites

Owing to its low recombination rate of electron-hole pairs, increased surface area, and excellent light absorption, the rGO/semiconductor nanocomposites' photocatalytic performance in the degradation of organic pollutants generally improves. Due to the integration of rGO, the adsorption of organic contaminants increases, thereby increasing decomposition efficiency. The improvement is due to the rapid and probable reaction of the adsorbed contaminants on rGO to the in situ replicated oxidative radicals. In photocatalysis, adsorption plays an important role because the active radical on the catalyst's surface will rapidly decompose the adsorbed organic molecules on the same surface. Strong rGO and semiconductor coupling results in good separation of charge; therefore, in situ semiconductor growth with rGO or vice versa will increase photocatalytic degradation due to enhanced electronic coupling between semiconductors and derivatives of rGO [95,96]. The higher photocurrent of the rGO and semiconductor composites also suggested the involvement of rGO in charged transport compared to pristine semiconductors. The widely understood mechanism is the rapid capture and transfer of photoexcited electrons by RGO from semiconductors [97]. In the presence of functional groups on the rGO surfaces, organic molecules may interact with the 2D structure of rGO through  $\pi$ - $\pi$  stacking and other weak or strong interactions, such as hydrogen bonding and electrostatic interaction, depending on the experimental parameters (pH, catalyst mass, pollutant concentration, and reaction time).

The photocatalytic mechanism of rGO/semiconductor has been studied by several research groups, such as Rahimi et al. [147], who proposed rGO/NiO nanowires for photocatalytic decomposition of methyl orange. They also established that the photocatalytic decomposition of methyl orange requires both hydroxide and superoxide radicals. The typical photocatalytic mechanism of the rGO/semiconductor composite for organic pollutant degradation has illustrated in Figure 6, where the light source with sufficient energy illuminated on the rGO/semiconductor and the formation of electron-hole pairs within the semiconductor structure can be represents by several steps as in the Equations (1)–(7) [148].

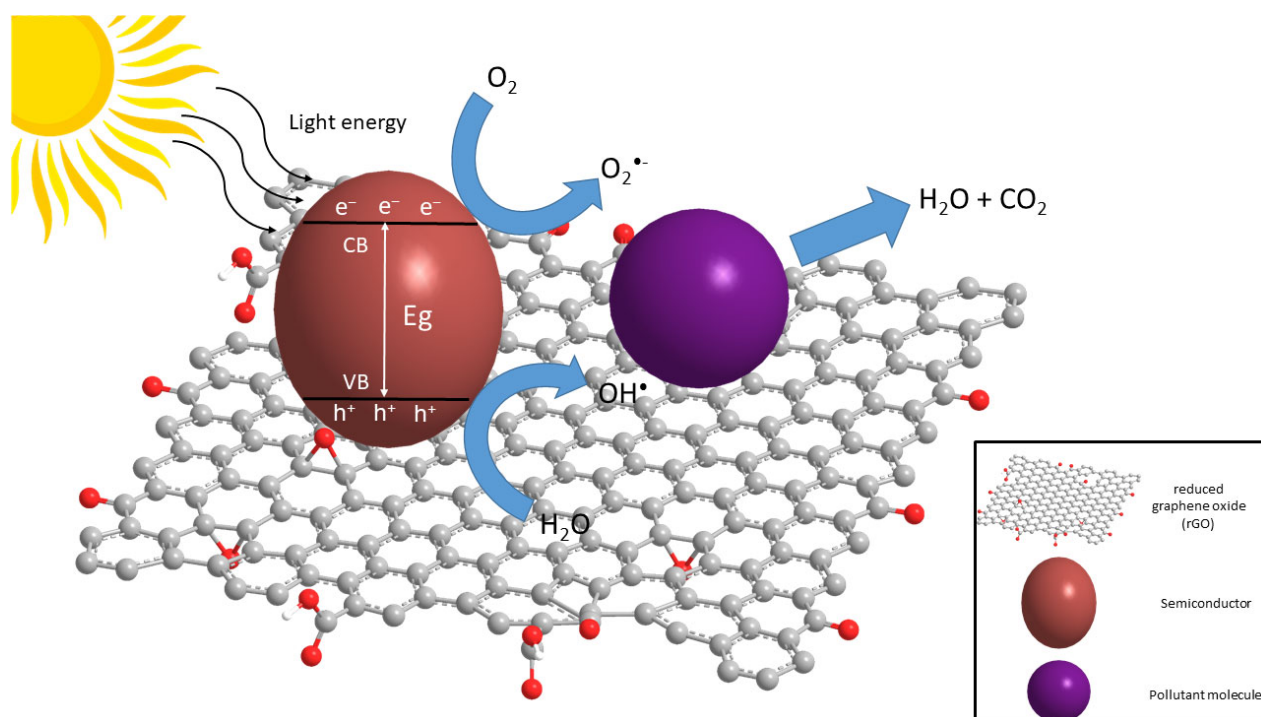
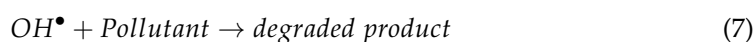
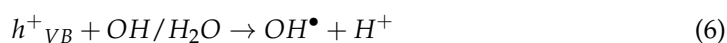
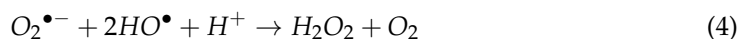
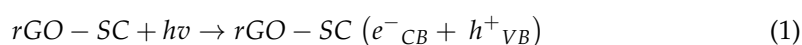


**Figure 6.** A proposed mechanism for the photodegradation of various organic pollutants over semiconductor-rGO composite under solar light irradiation.

Electron excitation to the conduction band that leaves the holes in the valance band (Equation (1)): the photoinduced electrons are then transferred to the rGO surfaces (Equation (2)), and these electrons are absorbed by the oxygen molecules and create superoxide radicals (Equation (3)) that can also be converted into hydroxide radicals (Equation (4) and (5)). These show that rGO plays a vital role in reducing the electron-hole pair recombination rate. Via an oxidative reaction (Equation (6)), the interaction between water molecules and holes creates hydroxyl radicals, and the radicals have a great oxidizing capacity that can degrade the targeted contaminants in water (Equation (7)) [148].



#### Scavenger's Test and Kinetics Studies

The electron-hole pairs and reactive oxygen species (ROS) such as hydroxyl radicals, singlet oxygen, and superoxide radicals are responsible for the degradation of the contaminants in most of the experiments conducted by the researchers. The presence of ROS was confirmed by the scavenger test and electron spin resonance analysis (ESR). The reactive oxygen species (ROS) used several chemicals as quenchers in the scavenger test. For example, isopropanol (IPA) as scavengers for hydroxyl radicals, 1,4-benzoquinone (BQ) as scavengers for superoxide radicals, and ethylenediaminetetraacetic acid disodium

salt (EDTA-2Na) as scavengers for holes are the quenchers used in the study conducted by Zhou et al. [149]. Other forms of chemicals, such as tert-butyl alcohol and ascorbic acid for hydroxyl radical [47,150] and potassium iodide for holes [47], have also been used as quenchers. The addition of these quenchers determines the active species in the photocatalytic degradation of the particular system in the scavenger test, as each system has numerous major reactive oxygen species that degrade the pollutants.

These quenchers prevent the ROS from reacting to the pollutant molecules and consequently reduce photodegradation's efficiency of the target pollutants. For example, In-, S-TiO<sub>2</sub>@rGO (In = Indium, S = Sulphur) was used as the photocatalyst for the degradation of atrazine, a form of pesticide used in agriculture in the work of Khavar et al. [151]. When the catalyst was irradiated, the process proposed by them absorbed the visible light energy and resulted in electron excitation that created photogenerated electron-hole pairs. The conduction band electrons were meant to be collected on the catalyst surface, and these electrons can be transferred to the rGO sheet with the presence of rGO in the system as it acts as a great electron acceptor. With dissolved oxygen molecules in the solution, the electrons on the rGO react and create superoxide radicals.

The electron can also be directly used on the catalyst's surface by the adsorbed oxygen molecules to produce other superoxide radicals. The holes of the valance band may also react with the hydroxide ion to create hydroxyl radicals or to degrade atrazine directly. It has been identified that hydroxyl radicals are the most reactive oxygen species involved in degradation. Salicylic acid and oxalate were used in the scavenger test as quenchers, and the number of hydroxyl radicals and holes was significantly reduced, thus reducing the efficiency of photocatalytic action.

Furthermore, as Chen et al. [152] described, the experiment was performed using rGO/TiO<sub>2</sub>/peroxodisulfate(PDS) for the degradation of diclofenac (DCF), an anti-inflammatory medication. The mechanism involved in the system is visible light energy activating the catalyst and forming photo-induced carriers that are electrons and holes. By further reducing the transfer resistance of the photogenerated charge carrier, rGO plays its role, and this inhibits the recombination of electrons and holes. Specifically, in this work, the valance band holes could not directly oxidize water molecules to create hydroxyl radicals because the TiO<sub>2</sub> valance band energy is +2.27 eV, which is lower than the +2.70 eV E<sub>H<sub>2</sub>O</sub>/·OH. Instead, by cleavage of the C–N bonds in molecules, the holes can directly degrade the DCF.

Peroxodisulfate (PDS) can absorb a portion of the conduction band electrons to create sulfate radical anions and react with water to produce hydroxyl radicals. The addition of PDS also helps improve the carrier charge separation. The dissolved oxygen reacts to another part of the conduction band electron, and the superoxide radicals are generated due to the lowest unoccupied molecular orbital radicals (LUMO) of rGO/TiO<sub>2</sub>, which was −0.39 eV, which was more extensive than E<sub>O<sub>2</sub>/O<sub>2</sub><sup>•−</sup></sub>, −0.33 eV. In the oxidized DCF anion and DCF molecules, which were in solution or on the catalyst surface, the superoxide radicals and singlet oxygen assisted in the system. Superoxide radical, electron, sulphate radical anion, and hydroxyl radical, involved in DCF mineralization, are the reactive oxygen species involved in the system.

Based on the above examples, it can be inferred that most of the previously mentioned photocatalytic degradation mechanisms are similar, even though the contaminants consist of various categories, such as antibiotics, dyes and pesticides. The reactive oxygen species produced, the availability of the oxidizing agent and the catalyst's properties were taken into account in the mechanism. The functions of rGO in the system as an electron acceptor and electron sink have also been clearly shown and can minimize the recombination rate. In addition, it also has excellent electronic conductivity to transfer the electron to its structure. In rGO composites, the conjugated sp<sup>2</sup> hybridized structure helps to delocalize electrons to facilitate the transport of photo-induced electrons. The rGO also helps to enhance the absorption of light and increase the number of molecules of the adsorption contaminants



on the catalyst's surface due to its large surface area. These demonstrate the synergistic impact of rGO in the composites of metal oxide/rGO.

To further study the system's photocatalytic process, the kinetics of photocatalytic activity must be determined to confirm whether they are zero-order, pseudo-first-order, or pseudo-second-order models. Most of the photocatalytic activities of metal oxides on organic pollutants show that the Langmuir-Hinshelwood (L-H) kinetic model can well describe the process and that the pseudo-first-order kinetics equation derived from the (L-H) kinetic model (Equation (8)) [153] was the best-fitted kinetic model used. The pseudo-first-order equation (Equation (9)) [153] that was used is as follows:

$$r = -\frac{dC}{dt} = \frac{k_r KC}{1 + KC'} \quad (8)$$

$$\ln \frac{C}{C_0} = -kt \quad (9)$$

where  $r$  represents the rate of reaction that changes with time,  $k_r$  and  $K$  are functions of  $C$  and  $C'$ , and  $C$  and  $C_0$  are the concentrations of pollutants at time  $t$  and 0. The pseudo-first-order reaction is a second-order reaction but has been modified to make it a first-order reaction that depends only on the concentration of one reactant and increasing the concentration of other reactants until in excess, so it does not affect the reaction. As stated in the work of Zhou et al. [153], the obtained humic acid removal data were fitted with Equation (9). Every data set's  $\ln(C/C_0)$  has a good linear relationship with  $t$ , indicating that the removal of humic acid obeys first-order kinetics. In addition, Shang et al. [124] also stated that the pseudo-first-order kinetics accompanied the degradation of perfluorooctanoic acid (PFOA) using Pb-BFO/rGO. With the pseudo-first-order kinetics equation, the degradation data had the best fit line.

## 5. Conclusions

As a viable alternative to enhancing photocatalytic efficiency in energy conversion applications, the construction of rGO semiconductor nanomaterials is gaining interest. This study explored a detailed review of current achievements in the fabrication of nanomaterials using rGO as photocatalysts in semiconductors and its design strategies for the degradation of various organic pollutants. Through various approaches such as hydrothermal, ultrasonic, co-precipitation, sol-gel, wet impregnation, electrospinning, ultrasonic spray pyrolysis, and electrophoretic, extensive research progress in the formation of nano-sized photocatalysts in the presence of rGO has been made. In particular, the implementation of rGO was able to overcome the constraints faced by the current pristine photocatalyst by reducing the recombination rate of charge carriers, raising the ability of adsorption, and increasing the range of light absorption. Therefore, it can be concluded that the positive hybridization of semiconductors with rGO elucidates results in enhancing the photocatalytic activity of semiconductors, especially in the treatment of wastewater, regardless of the type of contaminants and semiconductors used, based on the articles reviewed that published on the integration of semiconductor materials and rGO.

**Author Contributions:** N.H.M.K., A.F.R., S.T.; literature search, writing—original draft preparation and editing, R.A., M.L.I., S.F.M.Y.; writing—review and editing, N.H.M.K.; idea, supervision, writing—review and editing, N.H.M.K.—funding acquisition. All authors have read and agreed to the published version of the manuscript.

**Funding:** This research was funded by [Ministry of Higher Education] grant number [FRGS: 203/PKIMIA/6711792].

**Acknowledgments:** The authors would like to thank the ministry of Higher Education for the Fundamental Research Grant Scheme, FRGS (203/PKIMIA/6711792), and the Universiti Sains Malaysia.

**Conflicts of Interest:** The authors declare no conflict of interest.

## References

- Dunca, A.-M. Water pollution and water quality assessment of major transboundary rivers from Banat (Romania). *J. Chem.* **2018**, *2018*, 1–8. [\[CrossRef\]](#)
- Milanović, A.; Milijašević, D.; Brankov, J. Assessment of polluting effects and surface water quality using water pollution index: A case study of Hydro-system Danube-Tisa-Danube, Serbia. *Carpathian J. Earth Environ. Sci.* **2011**, *6*, 269–277.
- Chaudhary, M.; Walker, T.R. River Ganga pollution: Causes and failed management plans (correspondence on Dwivedi et al. 2018. Ganga water pollution: A potential health threat to inhabitants of Ganga basin. *Environment International* 117, 327–338). *Environ. Int.* **2019**, *126*, 202–206. [\[CrossRef\]](#) [\[PubMed\]](#)
- Wang, E.; Li, Q.; Hu, H.; Peng, F.; Zhang, P.; Li, J. Spatial characteristics and influencing factors of river pollution in China. *Water Environ. Res.* **2019**, *91*, 351–363. [\[CrossRef\]](#) [\[PubMed\]](#)
- Praveena, S.M.; Rashid, M.Z.M.; Nasir, F.A.M.; Yee, W.S.; Aris, A.Z. Occurrence and potential human health risk of pharmaceutical residues in drinking water from Putrajaya (Malaysia). *Ecotoxicol. Environ. Saf.* **2019**, *180*, 549–556. [\[CrossRef\]](#)
- Huang, Y.; Zhang, X.; Zhang, K.; Lu, P.; Zhang, D. Facile fabrication of sandwich-like BiOI/AgI/g-C<sub>3</sub>N<sub>4</sub> composites for efficient photocatalytic degradation of methyl orange and reduction of Cr(VI). *J. Nanoparticle Res.* **2018**, *20*, 328. [\[CrossRef\]](#)
- Walter, M.V.; Vennes, J.W. Occurrence of multiple-antibiotic-resistant enteric bacteria in domestic sewage and oxidation lagoons. *Appl. Environ. Microbiol.* **1985**, *50*, 930–933. [\[CrossRef\]](#) [\[PubMed\]](#)
- Gupta, G.; Kaur, A.; Sinha, A.S.K.; Kansal, S.K. Photocatalytic degradation of levofloxacin in aqueous phase using Ag/AgBr/BiOBr microplates under visible light. *Mater. Res. Bull.* **2017**, *88*, 148–155. [\[CrossRef\]](#)
- Hapeshi, E.; Achilleos, A.; Vasquez, M.; Michael, C.; Xekoukoulotakis, N.; Mantzavinos, D.; Kassinos, D. Drugs degrading photocatalytically: Kinetics and mechanisms of ofloxacin and atenolol removal on titania suspensions. *Water Res.* **2010**, *44*, 1737–1746. [\[CrossRef\]](#)
- Jones, K.C.; De Voogt, P. Persistent organic pollutants (POPs): State of the science. *Environ. Pollut.* **1999**, *100*, 209–221. [\[CrossRef\]](#)
- Jiang, J.-Q. The role of coagulation in water treatment. *Curr. Opin. Chem. Eng.* **2015**, *8*, 36–44. [\[CrossRef\]](#)
- Grassi, M.; Kaykioglu, G.; Belgiorio, V.; Lofrano, G. Emerging Compounds Removal from Wastewater. *Green Chem. Sustain.* Published online. **2012**, 15–38. [\[CrossRef\]](#)
- Ponraj, C.; Vinitha, G.; Daniel, J. A review on the visible light active BiFeO<sub>3</sub> nanostructures as suitable photocatalyst in the degradation of different textile dyes. *Environ. Nanotechnol. Monit. Manag.* **2017**, *7*, 110–120. [\[CrossRef\]](#)
- Deng, Y.; Zhao, R. Advanced oxidation processes (AOPs) in wastewater treatment. *Curr. Pollut. Rep.* **2015**, *1*, 167–176. [\[CrossRef\]](#)
- Glaze, W.H. Drinking-water treatment with ozone. *Environ. Sci. Technol.* **1987**, *21*, 224–230. [\[CrossRef\]](#) [\[PubMed\]](#)
- Hayati, F.; Isari, A.A.; Fattahi, M.; Anvaripour, B.; Jorfi, S. Photocatalytic decontamination of phenol and petrochemical wastewater through ZnO/TiO<sub>2</sub> decorated on reduced graphene oxide nanocomposite: Influential operating factors, mechanism, and electrical energy consumption. *RSC Adv.* **2018**, *8*, 40035–40053. [\[CrossRef\]](#)
- Lafi, W.K.; Shannak, B.; Al-Shannag, M.; Al-Anber, Z.; Al-Hasan, M. Treatment of olive mill wastewater by combined advanced oxidation and biodegradation. *Sep. Purif. Technol.* **2009**, *70*, 141–146. [\[CrossRef\]](#)
- Huang, C.; Dong, C.; Tang, Z. Advanced chemical oxidation: Its present role and potential future in hazardous waste treatment. *Waste Manag.* **1993**, *13*, 361–377. [\[CrossRef\]](#)
- Wammer, K.H.; Korte, A.R.; Lundeen, R.A.; Sundberg, J.E.; McNeill, K.; Arnold, W.A. Direct photochemistry of three fluoro-quinolone antibacterials: Norfloxacin, ofloxacin, and enrofloxacin. *Water Res.* **2013**, *47*, 439–448. [\[CrossRef\]](#) [\[PubMed\]](#)
- De Bel, E.; Dewulf, J.; De Witte, B.; Van Langenhove, H.; Janssen, C. Influence of pH on the sonolysis of ciprofloxacin: Biodegradability, ecotoxicity and antibiotic activity of its degradation products. *Chemosphere* **2009**, *77*, 291–295. [\[CrossRef\]](#)
- Michael, I.; Hapeshi, E.; Fattakassinos, D. Solar Fenton and solar TiO<sub>2</sub> catalytic treatment of ofloxacin in secondary treated effluents: Evaluation of operational and kinetic parameters. *Water Res.* **2010**, *44*, 5450–5462. [\[CrossRef\]](#)
- Hu, Z.-T.; Liu, J.; Yan, X.; Oh, W.-D.; Lim, T.-T. Low-temperature synthesis of graphene/Bi<sub>2</sub>Fe<sub>4</sub>O<sub>9</sub> composite for synergistic adsorption-photocatalytic degradation of hydrophobic pollutant under solar irradiation. *Chem. Eng. J.* **2015**, *262*, 1022–1032. [\[CrossRef\]](#)
- Zhu, M.; Zhai, C.; Fujitsuka, M.; Majima, T. Noble metal-free near-infrared-driven photocatalyst for hydrogen production based on 2D hybrid of black Phosphorus/WS<sub>2</sub>. *Appl. Catal. B Environ.* **2018**, *221*, 645–651. [\[CrossRef\]](#)
- Elmolla, E.S.; Chaudhuri, M. Degradation of amoxicillin, ampicillin and cloxacillin antibiotics in aqueous solution by the UV/ZnO photocatalytic process. *J. Hazard. Mater.* **2010**, *173*, 445–449. [\[CrossRef\]](#) [\[PubMed\]](#)
- Wang, X.; Wan, X.; Xu, X.; Chen, X. Facile fabrication of highly efficient AgI/ZnO heterojunction and its application of methylene blue and rhodamine B solutions degradation under natural sunlight. *Appl. Surf. Sci.* **2014**, *321*, 10–18. [\[CrossRef\]](#)
- Li, J.; Wang, Y.; Ling, H.; Qiu, Y.; Lou, J.; Hou, X.; Bag, S.P.; Wang, J.; Wu, H.; Chai, G. Significant Enhancement of the visible light photocatalytic properties in 3D BiFeO<sub>3</sub>/graphene composites. *Nanomaterials* **2019**, *9*, 65. [\[CrossRef\]](#) [\[PubMed\]](#)
- Soltani, T.; Tayyebi, A.; Lee, B.-K. Photolysis and photocatalysis of tetracycline by sonochemically heterojunctioned BiVO<sub>4</sub>/reduced graphene oxide under visible-light irradiation. *J. Environ. Manag.* **2019**, *232*, 713–721. [\[CrossRef\]](#) [\[PubMed\]](#)
- Praus, P.; Svoboda, L.; Dvorský, R.; Reli, M. Nanocomposites of SnO<sub>2</sub> and g-C<sub>3</sub>N<sub>4</sub>: Preparation, characterization and photocatalysis under visible LED irradiation. *Ceram. Int.* **2018**, *44*, 3837–3846. [\[CrossRef\]](#)

29. Kumar, S.; Ahmed, B.; Ojha, A.K.; Das, J.; Kumar, A. Facile synthesis of CdO nanorods and exploiting its properties towards supercapacitor electrode materials and low power UV irradiation driven photocatalysis against methylene blue dye. *Mater. Res. Bull.* **2017**, *90*, 224–231. [\[CrossRef\]](#)
30. Jaffari, Z.H.; Lam, S.-M.; Sin, J.-C.; Zeng, H. Boosting visible light photocatalytic and antibacterial performance by decoration of silver on magnetic spindle-like bismuth ferrite. *Mater. Sci. Semicond. Process.* **2019**, *101*, 103–115. [\[CrossRef\]](#)
31. Khalil, M.; Anggraeni, E.S.; Ivandini, T.A.; Budianto, E. Exposing TiO<sub>2</sub> (001) crystal facet in nano Au-TiO<sub>2</sub> heterostructures for enhanced photodegradation of methylene blue. *Appl. Surf. Sci.* **2019**, *487*, 1376–1384. [\[CrossRef\]](#)
32. Zayed, M.; Ahmed, A.M.; Shaban, M. Synthesis and characterization of nanoporous ZnO and Pt/ZnO thin films for dye degradation and water splitting applications. *Int. J. Hydrog. Energy* **2019**, *44*, 17630–17648. [\[CrossRef\]](#)
33. Mohamed, H.H. Sonochemical synthesis of ZnO hollow microstructure/reduced graphene oxide for enhanced sunlight photocatalytic degradation of organic pollutants. *J. Photochem. Photobiol. A Chem.* **2018**, *353*, 401–408. [\[CrossRef\]](#)
34. Saravanakumar, D.; Oualid, H.A.; Brahmi, Y.; Ayeshamariam, A.; Karunanaihy, M.; Saleem, A.M.; Kaviyarasu, K.; Sivaranjani, S.; Jayachandran, M. Synthesis and characterization of CuO/ZnO/CNTs thin films on copper substrate and its photocatalytic applications. *OpenNano* **2019**, *4*, 100025. [\[CrossRef\]](#)
35. Lee, K.; Yoon, H.; Ahn, C.; Park, J.; Jeon, S. Strategies to improve the photocatalytic activity of TiO<sub>2</sub>: 3D nanostructuring and heterostructuring with graphitic carbon nanomaterials. *Nanoscale* **2019**, *11*, 7025–7040. [\[CrossRef\]](#) [\[PubMed\]](#)
36. Mohan, S.; Sivakumar, B.; Kulangara, R.V.; Subramanian, B. Visible light driven photocatalytic efficiency of rGO-Ag-BiFeO<sub>3</sub> ternary nanohybrids on the decontamination of dye-polluted water: An amalgamation of 1D, 2D and 3D systems. *ChemistrySelect* **2016**, *1*, 6961–6971. [\[CrossRef\]](#)
37. Lee, S.-Y.; Park, S.-J. TiO<sub>2</sub> photocatalyst for water treatment applications. *J. Ind. Eng. Chem.* **2013**, *19*, 1761–1769. [\[CrossRef\]](#)
38. Zhang, G.; Song, A.; Duan, Y.; Zheng, S. Enhanced photocatalytic activity of TiO<sub>2</sub>/zeolite composite for abatement of pollutants. *Microporous Mesoporous Mater.* **2018**, *255*, 61–68. [\[CrossRef\]](#)
39. Zhang, T.; Liu, Y.; Rao, Y.; Li, X.; Yuan, D.; Tang, S.; Zhao, Q. Enhanced photocatalytic activity of TiO<sub>2</sub> with acetylene black and persulfate for degradation of tetracycline hydrochloride under visible light. *Chem. Eng. J.* **2020**, *384*, 123350. [\[CrossRef\]](#)
40. Pirzada, B.M.; Mir, N.A.; Qutub, N.; Mehraj, O.; Sabir, S.; Muneer, M. Synthesis, characterization and optimization of photocatalytic activity of TiO<sub>2</sub>/ZrO<sub>2</sub> nanocomposite heterostructures. *Mater. Sci. Eng. B* **2015**, *193*, 137–145. [\[CrossRef\]](#)
41. Guesh, K.; Mayoral, Á.; Márquez-Álvarez, C.; Chebude, Y.; Díaz, I. Enhanced photocatalytic activity of TiO<sub>2</sub> supported on zeolites tested in real wastewaters from the textile industry of Ethiopia. *Microporous Mesoporous Mater.* **2016**, *225*, 88–97. [\[CrossRef\]](#)
42. Jiang, Z.; Liu, Y.; Jing, T.; Huang, B.; Wang, Z.; Zhang, X.; Qin, X.; Dai, Y. Enhancing visible light photocatalytic activity of TiO<sub>2</sub> using a colorless molecule (2-methoxyethanol) due to hydrogen bond effect. *Appl. Catal. B: Environ.* **2017**, *200*, 230–236. [\[CrossRef\]](#)
43. Dorraj, M.; Goh, B.T.; Sairi, N.A.; Woi, P.M.; Basirun, W.J. Improved visible-light photocatalytic activity of TiO<sub>2</sub> co-doped with copper and iodine. *Appl. Surf. Sci.* **2018**, *439*, 999–1009. [\[CrossRef\]](#)
44. Ghugal, S.G.; Umare, S.S.; Sasikala, R. Enhanced photocatalytic activity of TiO<sub>2</sub> assisted by Nb, N and S multidopants. *Mater. Res. Bull.* **2015**, *61*, 298–305. [\[CrossRef\]](#)
45. Güy, N.; Özacar, M. The influence of noble metals on photocatalytic activity of ZnO for Congo red degradation. *Int. J. Hydrog. Energy* **2016**, *41*, 20100–20112. [\[CrossRef\]](#)
46. Karnan, T.; Selvakumar, S.A.S. Biosynthesis of ZnO nanoparticles using rambutan (*Nephelium lappaceum* L.) peel extract and their photocatalytic activity on methyl orange dye. *J. Mol. Struct.* **2016**, *1125*, 358–365. [\[CrossRef\]](#)
47. Vaizogullar, A.I. TiO<sub>2</sub>/ZnO supported on sepiolite: Preparation, structural characterization, and photocatalytic degradation of flumequine antibiotic in aqueous solution. *Chem. Eng. Commun.* **2017**, *204*, 689–697. [\[CrossRef\]](#)
48. Velanganni, S.; Pravinraj, S.; Immanuel, P.; Thiruneelakandan, R. Nanostructure CdS/ZnO heterojunction configuration for photocatalytic degradation of Methylene blue. *Phys. B: Condens. Matter* **2018**, *534*, 56–62. [\[CrossRef\]](#)
49. Ye, J.; Li, X.; Hong, J.; Chen, J.; Fan, Q. Photocatalytic degradation of phenol over ZnO nanosheets immobilized on montmorillonite. *Mater. Sci. Semicond. Process.* **2015**, *39*, 17–22. [\[CrossRef\]](#)
50. Dumitru, R.; Ianculescu, A.; Păcurariu, C.; Lupa, L.; Pop, A.; Vasile, B.; Surdu, A.; Manea, F. BiFeO<sub>3</sub>-synthesis, characterization and its photocatalytic activity towards doxorubicin degradation from water. *Ceram. Int.* **2019**, *45*, 2789–2802. [\[CrossRef\]](#)
51. Si, Y.-H.; Xia, Y.; Shang, S.-K.; Xiong, X.-B.; Zeng, X.-R.; Zhou, J.; Li, Y.-Y. Enhanced visible light driven photocatalytic behavior of BiFeO<sub>3</sub>/reduced graphene oxide composites. *Nanomaterials* **2018**, *8*, 526. [\[CrossRef\]](#) [\[PubMed\]](#)
52. Liu, P.; Sun, H.; Liu, X.; Sui, H.; Zhang, Y.; Zhou, D.; Guo, Q.; Ruan, Y. Enhanced photocatalytic performance of Bi<sub>2</sub>Fe<sub>4</sub>O<sub>9</sub>/graphene via modifying graphene composite. *J. Am. Ceram. Soc.* **2017**, *100*, 3540–3549. [\[CrossRef\]](#)
53. Basith, M.A.; Ahsan, R.; Zarin, I.; Jalil, M.A. Enhanced photocatalytic dye degradation and hydrogen production ability of Bi<sub>25</sub>FeO<sub>40</sub>-rGO nanocomposite and mechanism insight. *Sci. Rep.* **2018**, *8*, 1–11. [\[CrossRef\]](#)
54. Zhang, L.; Zhang, X.; Zou, Y.; Xu, Y.-H.; Pan, C.-L.; Hu, J.-S.; Hou, C.-M. Hydrothermal synthesis, influencing factors and excellent photocatalytic performance of novel nanoparticle-assembled Bi<sub>25</sub>FeO<sub>40</sub> tetrahedrons. *CrystEngComm* **2015**, *17*, 6527–6537. [\[CrossRef\]](#)
55. Malathi, A.; Arunachalam, P.; Kirankumar, V.; Madhavan, J.; Al-Mayouf, A.M. An efficient visible light driven bismuth ferrite incorporated bismuth oxyiodide (BiFeO<sub>3</sub>/BiOI) composite photocatalytic material for degradation of pollutants. *Opt. Mater.* **2018**, *84*, 227–235. [\[CrossRef\]](#)

56. Arshad, A.; Iqbal, J.; Siddiq, M.; Mansoor, Q.; Ismail, M.; Mehmood, F.; Ajmal, M.; Abid, Z. Graphene nanoplatelets induced tailoring in photocatalytic activity and antibacterial characteristics of MgO/graphene nanoplatelets nanocomposites. *J. Appl. Phys.* **2017**, *121*, 024901. [[CrossRef](#)]
57. Panchal, P.; Paul, D.R.; Sharma, A.; Hooda, D.; Yadav, R.; Meena, P.; Nehra, S. Phytoextract mediated ZnO/MgO nanocomposites for photocatalytic and antibacterial activities. *J. Photochem. Photobiol. A Chem.* **2019**, *385*, 112049. [[CrossRef](#)]
58. Arshad, A.; Iqbal, J.; Siddiq, M.; Ali, M.U.; Ali, A.; Shabbir, H.; Bin Nazeer, U.; Saleem, M.S. Solar light triggered catalytic performance of graphene-CuO nanocomposite for waste water treatment. *Ceram. Int.* **2017**, *43*, 10654–10660. [[CrossRef](#)]
59. Mageshwari, K.; Nataraj, D.; Pal, T.; Sathyamoorthy, R.; Park, J. Improved photocatalytic activity of ZnO coupled CuO nanocomposites synthesized by reflux condensation method. *J. Alloy. Compd.* **2015**, *625*, 362–370. [[CrossRef](#)]
60. Arunadevi, R.; Kavitha, B.; Rajarajan, M.; Suganthi, A.; Jeyamurugan, A. Investigation of the drastic improvement of photocatalytic degradation of Congo red by monoclinic Cd, Ba-CuO nanoparticles and its antimicrobial activities. *Surf. Interfaces* **2018**, *10*, 32–44. [[CrossRef](#)]
61. Zhu, W.; Sun, F.; Goei, R.; Zhou, Y. Facile fabrication of RGO-WO<sub>3</sub> composites for effective visible light photocatalytic degradation of sulfamethoxazole. *Appl. Catal. B Environ.* **2017**, *207*, 93–102. [[CrossRef](#)]
62. Cao, Q.W.; Zheng, Y.F.; Song, X.C. Enhanced visible-light-driven photocatalytic degradation of RhB by AgIO<sub>3</sub>/WO<sub>3</sub> composites. *J. Taiwan Inst. Chem. Eng.* **2017**, *70*, 359–365. [[CrossRef](#)]
63. Hakimi, M.; Morvaridi, M.; Hosseini, H.A.; Alimard, P. Preparation, characterization, and photocatalytic activity of Bi<sub>2</sub>O<sub>3</sub>-Al<sub>2</sub>O<sub>3</sub> nanocomposite. *Polyhedron* **2019**, *170*, 523–529. [[CrossRef](#)]
64. Reyes-Coronado, D.; Rodriguez-Gattorno, G.; Espinosa-Pesqueira, M.E.; Cab, C.; De Coss, R.; Oskam, G. Phase-pure TiO<sub>2</sub> nanoparticles: Anatase, brookite and rutile. *Nanotechnol.* **2008**, *19*, 145605. [[CrossRef](#)]
65. Lee, K.M.; Lai, C.W.; Ngai, K.S.; Juan, J.C. Recent developments of zinc oxide based photocatalyst in water treatment technology: A review. *Water Res.* **2016**, *88*, 428–448. [[CrossRef](#)] [[PubMed](#)]
66. Daneshvar, N.; Salari, D.; Khataee, A. Photocatalytic degradation of azo dye acid red 14 in water on ZnO as an alternative catalyst to TiO<sub>2</sub>. *J. Photochem. Photobiol. A Chem.* **2004**, *162*, 317–322. [[CrossRef](#)]
67. Behnajady, M.A.; Modirshahla, N.; Hamzavi, R.; Kinetic study on photocatalytic degradation of C.I. Acid Yellow 23 by ZnO photocatalyst. *J. Hazard. Mater.* **2006**, *133*, 226–232. [[CrossRef](#)]
68. Vimercati, L.; Cavone, D.; Caputi, A.; De Maria, L.; Tria, M.; Prato, E.; Ferri, G.M. Nanoparticles: An experimental study of zinc nanoparticles toxicity on marine crustaceans. General overview on the health implications in humans. *Front. Public Heal.* **2020**, *8*, 1–19. [[CrossRef](#)]
69. Monsé, C.; Hagemeyer, O.; Raulf, M.; Jettkant, B.; Van Kampen, V.; Kendzia, B.; Gering, V.; Kappert, G.; Weiss, T.; Ulrich, N.; et al. Concentration-dependent systemic response after inhalation of nano-sized zinc oxide particles in human volunteers. *Part. Fibre Toxicol.* **2018**, *15*, 1–11. [[CrossRef](#)]
70. Mojir Shaibani, P.M.; Prashanthi, K.; Sohrabi, A.; Thundat, T. Photocatalytic BiFeO<sub>3</sub> nanofibrous mats for effective water treatment. *J. Nanotechnol.* **2013**, *2013*, 1–6. [[CrossRef](#)]
71. Li, T.; Shen, J.; Li, N.; Ye, M. Hydrothermal preparation, characterization and enhanced properties of reduced graphene-BiFeO<sub>3</sub> nanocomposite. *Mater. Lett.* **2013**, *91*, 42–44. [[CrossRef](#)]
72. Roy, S.; Majumder, S. Recent advances in multiferroic thin films and composites. *J. Alloy. Compd.* **2012**, *538*, 153–159. [[CrossRef](#)]
73. Lian, J.; Zhang, C.; Wang, P.; Ng, D.H.L. Template-free hydrothermal synthesis of mesoporous MgO nanostructures and their applications in water treatment. *Chem. Asian J.* **2012**, *7*, 2650–2655. [[CrossRef](#)] [[PubMed](#)]
74. Casillas, J.E.; Campa-Molina, J.; Tzompantzi, F.; Arizaga, G.G.C.; López-Gaona, A.; Ulloa-Godínez, S.; Cano, M.E.; Barrera, A. Photocatalytic degradation of diclofenac using Al<sub>2</sub>O<sub>3</sub>-Nd<sub>2</sub>O<sub>3</sub> binary oxides prepared by the sol-gel method. *Materials* **2020**, *13*, 1345. [[CrossRef](#)] [[PubMed](#)]
75. Meyer, B.K.; Polity, A.; Reppin, D.; Becker, M.; Hering, P.; Klar, P.J.; Sander, T.; Reindl, C.; Benz, J.; Eichhoff, M.; et al. Binary copper oxide semiconductors: From materials towards devices. *Physica Status Solidi B* **2012**, *249*, 1487–1509. [[CrossRef](#)]
76. Shi, G.; Liu, J.; Chen, B.; Bao, Y.; Xu, J. Phase-controlled growth of cubic phase CuO nanoparticles by chemical vapor deposition. *Physica Status Solidi A* **2017**, *214*. [[CrossRef](#)]
77. Sathyamoorthy, R.; Mageshwari, K.; Mali, S.S.; Priyadharshini, S.; Patil, P.S. Effect of organic capping agent on the photocatalytic activity of MgO nanoflakes obtained by thermal decomposition route. *Ceram. Int.* **2013**, *39*, 323–330. [[CrossRef](#)]
78. Camacho, L.M.; Torres, A.; Saha, D.; Deng, S. Adsorption equilibrium and kinetics of fluoride on sol-gel-derived activated alumina adsorbents. *J. Colloid Interface Sci.* **2010**, *349*, 307–313. [[CrossRef](#)]
79. Gaudet, J.R.; De La Riva, A.; Peterson, E.J.; Bolin, T.; Datye, A.K. Improved low-temperature CO oxidation performance of Pd supported on La-stabilized alumina. *ACS Catal.* **2013**, *3*, 846–855. [[CrossRef](#)]
80. Ealet, B.; Elyakhloufi, M.; Gillet, E.; Ricci, M. Electronic and crystallographic structure of  $\gamma$ -alumina thin films. *Thin Solid Films* **1994**, *250*, 92–100. [[CrossRef](#)]
81. Weng, B.; Wu, J.; Zhang, N.; Xu, Y.-J. Observing the role of graphene in boosting the two-electron reduction of oxygen in graphene-WO<sub>3</sub> nanorod photocatalysts. *Langmuir* **2014**, *30*, 5574–5584. [[CrossRef](#)] [[PubMed](#)]
82. Rao, C.M. Structure and properties of WO<sub>3</sub> thin films for electrochromic device application. *J. Non Oxide Glasses* **2013**, *5*, 1–8.
83. Allen, M.J.; Tung, V.C.; Kaner, R.B. Honeycomb carbon: A review of graphene. *Chem. Rev.* **2010**, *110*, 132–145. [[CrossRef](#)]



84. Hu, C.; Lu, T.; Chen, F.; Zhang, R. A brief review of graphene–metal oxide composites synthesis and applications in photocatalysis. *J. Chin. Adv. Mater. Soc.* **2013**, *1*, 21–39. [\[CrossRef\]](#)
85. Poh, H.L.; Šaněk, F.; Ambrosi, A.; Zhao, G.; Sofer, Z.; Pumera, M. Graphenes prepared by Staudenmaier, Hofmann and Hummers methods with consequent thermal exfoliation exhibit very different electrochemical properties. *Nanoscale* **2012**, *4*, 3515–3522. [\[CrossRef\]](#)
86. Novoselov, K.S.; Geim, A.K.; Morozov, S.V.; Jiang, D.; Katsnelson, M.I.; Grigorieva, I.V.; Dubonos, S.V.; Firsov, A.A. Two-dimensional gas of massless Dirac fermions in graphene. *Nature* **2005**, *438*, 197–200. [\[CrossRef\]](#) [\[PubMed\]](#)
87. Johra, F.T.; Jung, W. RGO-TiO<sub>2</sub>-ZnO composites: Synthesis, characterization, and application to photocatalysis. *Appl. Catal. A Gen.* **2015**, *491*, 52–57.
88. Li, N.; Zheng, M.; Lu, H.; Hu, Z.; Shen, C.; Chang, X.; Ji, G.; Cao, J.; Shi, Y. High-rate lithium–sulfur batteries promoted by reduced graphene oxide coating. *Chem. Commun.* **2012**, *48*, 4106–4108. [\[CrossRef\]](#) [\[PubMed\]](#)
89. Firmiano, E.G.S.; Cordeiro, M.A.L.; Rabelo, A.C.; Dalmaschio, C.J.; Pinheiro, A.N.; Pereira, E.C.; Leite, E.R. Graphene oxide as a highly selective substrate to synthesize a layered MoS<sub>2</sub> hybrid electrocatalyst. *Chem. Commun.* **2012**, *48*, 7687–7689. [\[CrossRef\]](#) [\[PubMed\]](#)
90. Yin, Z.; Sun, S.; Salim, T.; Wu, S.; Huang, X.; He, Q.; Lam, Y.M.; Zhang, H. Organic photovoltaic devices using highly flexible reduced graphene oxide films as transparent electrodes. *ACS Nano* **2010**, *4*, 5263–5268. [\[CrossRef\]](#) [\[PubMed\]](#)
91. Pant, H.R.; Pant, B.; Kim, H.J.; Amarjargal, A.; Park, C.H.; Tijjing, L.D.; Kim, E.K.; Kim, C.S. A green and facile one-pot synthesis of Ag-ZnO/RGO nanocomposite with effective photocatalytic activity for removal of organic pollutants. *Ceram. Int.* **2013**, *39*, 5083–5091. [\[CrossRef\]](#)
92. Wang, W.; Han, Q.; Zhu, Z.; Zhang, L.; Zhong, S.; Liu, B. Enhanced photocatalytic degradation performance of organic contaminants by heterojunction photocatalyst BiVO<sub>4</sub>/TiO<sub>2</sub>/RGO and its compatibility on four different tetracycline antibiotics. *Adv. Powder Technol.* **2019**, *30*, 1882–1896. [\[CrossRef\]](#)
93. Wu, D.; Su, X.; Guo, W. Enhanced photocatalytic degradation of methylene blue over hexagonal WO<sub>3</sub>/graphene under visible-light irradiation. *Kinet. Catal.* **2017**, *58*, 710–719. [\[CrossRef\]](#)
94. Wang, H.; Zhang, N.; Cheng, G.; Guo, H.; Shen, Z.; Yang, L.; Zhao, Y.; Alsaedi, A.; Hayat, T.; Wang, X. Preparing a photocatalytic Fe doped TiO<sub>2</sub>/rGO for enhanced bisphenol A and its analogues degradation in water sample. *Appl. Surf. Sci.* **2020**, *505*, 144640. [\[CrossRef\]](#)
95. Dong, S.; Li, Y.; Sun, J.; Yu, C.; Li, Y.; Sun, J. Facile synthesis of novel ZnO/RGO hybrid nanocomposites with enhanced catalytic performance for visible-light-driven photodegradation of metronidazole. *Mater. Chem. Phys.* **2014**, *145*, 357–365. [\[CrossRef\]](#)
96. Raja, A.; Rajasekaran, P.; Selvakumar, K.; Arunpandian, M.; Kaviyarasu, K.; Bahadur, S.A.; Swaminathan, M. Visible active reduced graphene oxide-BiVO<sub>4</sub>-ZnO ternary photocatalyst for efficient removal of ciprofloxacin. *Sep. Purif. Technol.* **2020**, *233*, 115996. [\[CrossRef\]](#)
97. Li, K.; Chen, T.; Yan, L.; Dai, Y.; Huang, Z.; Xiong, J.; Song, D.; Lv, Y.; Zeng, Z. Design of graphene and silica co-doped titania composites with ordered mesostructure and their simulated sunlight photocatalytic performance towards atrazine degradation. *Colloids Surf. A Physicochem. Eng. Asp.* **2013**, *422*, 90–99. [\[CrossRef\]](#)
98. Wang, Z.; Wang, Y.; Huang, L.; Liu, X.; Han, Y.; Wang, L. La<sub>2</sub>Zr<sub>2</sub>O<sub>7</sub>/rGO synthesized by one-step sol-gel method for photocatalytic degradation of tetracycline under visible-light. *Chem. Eng. J.* **2020**, *384*, 123380. [\[CrossRef\]](#)
99. Prabhakar Rao, N.; Chandra, M.R.; Rao, T.S. Synthesis of Zr doped TiO<sub>2</sub>/reduced Graphene Oxide (rGO) nanocomposite material for efficient photocatalytic degradation of eosin blue dye under visible light irradiation. *J. Alloy. Compd.* **2017**, *694*, 596–606. [\[CrossRef\]](#)
100. Soltani, T.; Lee, B.K. Sono-synthesis of nanocrystallized BiFeO<sub>3</sub>/reduced graphene oxide composites for visible photocatalytic degradation improvement of bisphenol A. *Chem. Eng. J.* **2016**, *306*, 204–213. [\[CrossRef\]](#)
101. Peng, Y.; Ji, J.; Chen, D. Ultrasound assisted synthesis of ZnO/reduced graphene oxide composites with enhanced photocatalytic activity and anti-photocorrosion. *Appl. Surf. Sci.* **2015**, *356*, 762–768. [\[CrossRef\]](#)
102. Babu, S.G.; Karthik, P.; John, M.C.; Lakhera, S.K.; AshokKumar, M.; Khim, J.; Neppolian, B. Synergistic effect of sono-photocatalytic process for the degradation of organic pollutants using CuO-TiO<sub>2</sub>/rGO. *Ultrason. Sonochemistry* **2019**, *50*, 218–223. [\[CrossRef\]](#)
103. Labhane, P.; Patle, L.; Huse, V.; Sonawane, G. Synthesis of reduced graphene oxide sheets decorated by zinc oxide nanoparticles: Crystallographic, optical, morphological and photocatalytic study. *Chem. Phys. Lett.* **2016**, *661*, 13–19. [\[CrossRef\]](#)
104. Moitra, D.; Chandel, M.; Ghosh, B.K.; Jani, R.K.; Patra, M.K.; Vadera, S.R.; Ghosh, N.N. A simple ‘in situ’ co-precipitation method for the preparation of multifunctional CoFe<sub>2</sub>O<sub>4</sub>-reduced graphene oxide nanocomposites: Excellent microwave absorber and highly efficient magnetically separable recyclable photocatalyst for dye degradation. *RSC Adv.* **2016**, *6*, 76759–76772. [\[CrossRef\]](#)
105. Rahmat, S.T.; Tan, W.K.; Kawamura, G.; Matsuda, A.; Lockman, Z. Facile fabrication of rGO/Rutile TiO<sub>2</sub> nanowires as photocatalyst for Cr(VI) Reduction. *Mater. Today Proc.* **2019**, *17*, 1143–1151. [\[CrossRef\]](#)
106. Kumar, G.; Nikolla, E.; Linic, S.; Medlin, J.W.; Janik, M.J. Multicomponent catalysts: Limitations and prospects. *ACS Catal.* **2018**, *8*, 3202–3208. [\[CrossRef\]](#)
107. Noormohammadi, E.; Sanjabi, S. Photocatalytic activity and wettability of rGO/TiO<sub>2</sub> nanocomposites prepared by electrophoretic co-deposition. *Surf. Rev. Lett.* **2019**, *27*, 9–11. [\[CrossRef\]](#)
108. Ramos, P.G.; Luyo, C.; Sánchez, L.A.; Gomez, E.D.; Rodriguez, J.M. The spinning voltage influence on the growth of ZnO-rGO nanorods for photocatalytic degradation of methyl orange dye. *Catalysts* **2020**, *10*, 660. [\[CrossRef\]](#)



109. Park, J.A.; Yang, B.; Lee, J.; Kim, I.G.; Kim, J.-H.; Choi, J.-W.; Park, H.-D.; Nah, I.W.; Lee, S.-H. Ultrasonic spray pyrolysis synthesis of reduced graphene oxide/anatase TiO<sub>2</sub> composite and its application in the photocatalytic degradation of methylene blue in water. *Chemosphere* **2018**, *191*, 738–746. [CrossRef]
110. Prabhu, S.; Pudukudy, M.; Sohila, S.; Harish, S.; Navaneethan, M.; Ramesh, R.; Hayakawa, Y. Synthesis, structural and optical properties of ZnO spindle/reduced graphene oxide composites with enhanced photocatalytic activity under visible light irradiation. *Opt. Mater.* **2018**, *79*, 186–195. [CrossRef]
111. Sharma, A.; Lee, B.-K. Integrated ternary nanocomposite of TiO<sub>2</sub>/NiO/reduced graphene oxide as a visible light photocatalyst for efficient degradation of o-chlorophenol. *J. Environ. Manag.* **2016**, *181*, 563–573. [CrossRef]
112. Zhu, J.; Zhu, Z.; Zhang, H.; Lu, H.; Zhang, W.; Qiu, Y.; Zhu, L.; Küppers, S. Calcined layered double hydroxides/reduced graphene oxide composites with improved photocatalytic degradation of paracetamol and efficient oxidation-adsorption of As(III). *Appl. Catal. B Environ.* **2018**, *225*, 550–562. [CrossRef]
113. Sharma, P.; Kumar, N.; Chauhan, R.; Singh, V.; Srivastava, V.C.; Bhatnagar, R. Growth of hierarchical ZnO nano flower on large functionalized rGO sheet for superior photocatalytic mineralization of antibiotic. *Chem. Eng. J.* **2020**, *392*, 123746. [CrossRef]
114. Ranjith, R.; Renganathan, V.; Chen, S.-M.; Selvan, N.S.; Rajam, P.S. Green synthesis of reduced graphene oxide supported TiO<sub>2</sub>/Co<sub>3</sub>O<sub>4</sub> nanocomposite for photocatalytic degradation of methylene blue and crystal violet. *Ceram. Int.* **2019**, *45*, 12926–12933. [CrossRef]
115. Li, A.D.; Liu, W.C. Optical properties of ferroelectric nanocrystal/polymer composites. *Phys. Prop. Appl. Polym. Nanocompos.* Published online. **2010**, 108–158. [CrossRef]
116. Xu, H.Y.; Wang, H.; Zhang, Y.C.; He, W.L.; Zhu, M.K.; Wang, B.; Yan, H. Hydrothermal synthesis of zinc oxide powders with controllable morphology. *Ceramic Int.* **2011**, *1*, 93–97. [CrossRef]
117. O'Hare, D. Hydrothermal synthesis. *Encycl. Mater. Sci. Technol.* Published online. **2001**, 3989–3992. [CrossRef]
118. Ruidiaz-Martínez, M.; Álvarez, M.A.; López-Ramón, M.V.; Cruz-Quesada, G.; Rivera-Utrilla, J.; Sánchez-Polo, M. Hydrothermal synthesis of rGO-TiO<sub>2</sub> composites as high-performance UV photocatalysts for ethylparaben degradation. *Catalysts* **2020**, *10*, 520. [CrossRef]
119. Wang, P.; Wang, J.; Wang, X.; Yu, H.; Yu, J.; Lei, M.; Wang, Y. One-step synthesis of easy-recycling TiO<sub>2</sub>-rGO nanocomposite photocatalysts with enhanced photocatalytic activity. *Appl. Catal. B Environ.* **2013**, *133*, 452–459. [CrossRef]
120. Lv, K.; Fang, S.; Si, L.; Xia, Y.; Ho, W.; Li, M. Fabrication of TiO<sub>2</sub> nanorod assembly grafted rGO (rGO@TiO<sub>2</sub>-NR) hybridized flake-like photocatalyst. *Appl. Surf. Sci.* **2017**, *391*, 218–227. [CrossRef]
121. Wang, H.; Wang, G.; Zhang, Y.; Ma, Y.; Zhang, Q.; Pu, H.; Xu, W.; Gao, D.; Wang, B.; Qi, X. Preparation of RGO/TiO<sub>2</sub> photocatalyst and the mechanism of its hydrothermal process. *J. Chin. Chem. Soc.* **2019**, *66*, 734–739. [CrossRef]
122. Tolosana-Moranchel, Á.; Manassero, A.; Satuf, M.L.; Alfano, O.M.; Casas, J.A.; Bahamonde, A. TiO<sub>2</sub>-rGO photocatalytic degradation of an emerging pollutant: Kinetic modelling and determination of intrinsic kinetic parameters. *J. Environ. Chem. Eng.* **2019**, *7*, 103406. [CrossRef]
123. Romeiro, F.C.; Rodrigues, M.A.; Silva, L.A.; Catto, A.C.; da Silva, L.F.; Longo, E.; Nossol, E.; Lima, R.C. rGO-ZnO nanocomposites for high electrocatalytic effect on water oxidation obtained by microwave-hydrothermal method. *Appl. Surf. Sci.* **2017**, *423*, 743–751. [CrossRef]
124. Shang, E.; Li, Y.; Niu, J.; Li, S.; Zhang, G.; Wang, X. Photocatalytic degradation of perfluorooctanoic acid over Pb-BiFeO<sub>3</sub>/rGO catalyst: Kinetics and mechanism. *Chemosphere* **2018**, *211*, 34–43. [CrossRef] [PubMed]
125. Khamboonruang, D.; Srirattanapibul, S.; Tang, I.-M.; Thongmee, S. TiO<sub>2</sub>-rGO nanocomposite as a photo catalyst for the reduction of Cr<sup>6+</sup>. *Mater. Res. Bull.* **2018**, *107*, 236–241. [CrossRef]
126. Srirattanapibul, S.; Tang, I.-M.; Thongmee, S. Photo catalytic reduction of Cr<sup>6+</sup> by ZnO decorated on reduced graphene oxide (rGO) Nanocomposites. *Mater. Res. Bull.* **2020**, *122*. [CrossRef]
127. Han, F.; Li, H.; Yang, J.; Cai, X.; Fu, L. One-pot synthesis of cuprous oxide-reduced graphene oxide nanocomposite with enhanced photocatalytic and electrocatalytic performance. *Physica E Low Dimens. Syst. Nanostructures* **2016**, *77*, 122–126. [CrossRef]
128. Zhigang, N. Reduced graphene oxide-cuprous oxide hybrid nanopowders: Hydrothermal synthesis and enhanced photocatalytic performance under visible light irradiation. *Mater. Sci. Semicond. Process.* **2014**, *23*, 78–84. [CrossRef]
129. Sun, L.; Wang, G.; Hao, R.; Han, D.; Cao, S. Solvothermal fabrication and enhanced visible light photocatalytic activity of Cu<sub>2</sub>O-reduced graphene oxide composite microspheres for photodegradation of Rhodamine, B. *Appl. Surf. Sci.* **2015**, *358*, 91–99. [CrossRef]
130. Zou, W.; Zhang, L.; Liu, L.; Wang, X.; Sun, J.; Wu, S.; Deng, Y.; Tang, C.; Gao, F.; Dong, L. Engineering the Cu<sub>2</sub>O-reduced graphene oxide interface to enhance photocatalytic degradation of organic pollutants under visible light. *Appl. Catal. B Environ.* **2016**, *181*, 495–503. [CrossRef]
131. Cauqui, M.A.; Rodríguez-Izquierdo, J.M. Application of the sol-gel methods to catalyst preparation. *J. Non Cryst. Solids* **1992**, *92*, 724–738. [CrossRef]
132. Banerjee, S.; Benjwal, P.; Singh, M.; Kar, K.K. Graphene oxide (rGO)-metal oxide (TiO<sub>2</sub>/Fe<sub>3</sub>O<sub>4</sub>) based nanocomposites for the removal of methylene blue. *Appl. Surf. Sci.* **2018**, *439*, 560–568. [CrossRef]
133. Alizadeh, S.; Fallah, N.; Nikazar, M. An ultrasonic method for the synthesis, control and optimization of CdS/TiO<sub>2</sub> core-shell nanocomposites. *RSC Adv.* **2019**, *9*, 4314–4324. [CrossRef]

134. Deshmukh, S.P.; Kale, D.P.; Kar, S.; Shirsath, S.R.; Bhanvase, B.A.; Saharan, V.K.; Sonawane, S.H. Ultrasound assisted preparation of rGO/TiO<sub>2</sub> nanocomposite for effective photocatalytic degradation of methylene blue under sunlight. *Nano Struct. Nano Objects* **2020**, *21*, 100407. [\[CrossRef\]](#)
135. Deraz, N.M. The comparative jurisprudence of catalysts preparation methods: I. precipitation and impregnati. *J. Ind. Environ. Chem.* **2018**, *2*, 19–21.
136. Sietsma, J.R.; Van Dillen, A.J.; De Jongh, P.E.; De Jong, K.P. Application of ordered mesoporous materials as model supports to study catalyst preparation by impregnation and drying. *Stud. Surf. Sci. Catal.* **2006**, *162*, 95–102.
137. Haber, J.; Block, J.H.; Delmon, B. Manual of methods and procedures for catalyst characterization. *Pure Appl. Chem.* **1995**, *67*, 1257–1306. [\[CrossRef\]](#)
138. Babu, S.G.; Vinoth, R.; Neppolian, B.; Dionysiou, D.D.; AshokKumar, M. Diffused sunlight driven highly synergistic pathway for complete mineralization of organic contaminants using reduced graphene oxide supported photocatalyst. *J. Hazard. Mater.* **2015**, *291*, 83–92. [\[CrossRef\]](#) [\[PubMed\]](#)
139. Bellardita, M.; Di Paola, A.; Yurdakal, S.; Palmisano, L. Chapter 2—Preparation of Catalysts and Photocatalysts Used for Similar Processes. In *Heterogeneous Photocatalysis*; Marci, G., Palmisano, L., Eds.; Springer: Berlin, Germany, 2019; pp. 25–56. [\[CrossRef\]](#)
140. Pouya, A.; Jerzy, S.; Krasinski, R.V.; Lobat, T.; Vashae, D. Electrophoretic Deposition (EPD): 17 Fundamentals and Applications from Nano- to Microscale Structures. In *Handbook of Nanoelectrochemistry*; Aliofkhazraei, M., Hamdy Makhoulouf, A.S., Eds.; Springer International Publishing: Cham, Switzerland, 2016. [\[CrossRef\]](#)
141. Besra, L.; Liu, M. A review on fundamentals and applications of electrophoretic deposition (EPD). *Prog. Mater. Sci.* **2007**, *52*, 1–61. [\[CrossRef\]](#)
142. Reddy, A.B.; Reddy, G.S.M.; Sivanjineyulu, V.; Jayaramudu, J.; Varaprasad, K.; Sadiku, E.R. Hydrophobic/Hydrophilic Nanostructured Polymer Blends. In *Micro and Nano Technologies, Design and Applications of Nanostructured Polymer Blends and Nanocomposite Systems*; Thomas, S., Shanks, R., Chandrasekharakurup, S., Eds.; William Andrew Publishing: Norwich, NY, USA, 2016; pp. 385–411. [\[CrossRef\]](#)
143. Xue, J.; Wu, T.; Dai, Y.; Xia, Y. Electrospinning and electrospun nanofibers: Methods, materials, and applications. *Chem. Rev.* **2019**, *119*, 5298–5415. [\[CrossRef\]](#)
144. Messing, G.L.; Zhang, S.-C.; Jayanthi, G.V. Ceramic powder synthesis by spray pyrolysis. *J. Am. Ceram. Soc.* **1993**, *76*, 2707–2726. [\[CrossRef\]](#)
145. Tsai, S.C.; Song, Y.L.; Tsai, C.S.; Chiu, W.Y.; Lin, H.M. Ultrasonic spray pyrolysis for nanoparticles synthesis. *Mater. Sci.* **2004**, *39*, 3647–3657. [\[CrossRef\]](#)
146. Ardekani, S.R.; Aghdam, A.S.R.; Nazari, M.; Bayat, A.; Yazdani, E.; Saievar-Iranizad, E. A comprehensive review on ultrasonic spray pyrolysis technique: Mechanism, main parameters and applications in condensed matter. *J. Anal. Appl. Pyrolysis* **2019**, *141*, 104631. [\[CrossRef\]](#)
147. Rahimi, K.; Zafarkish, H.; Yazdani, A. Reduced graphene oxide can activate the sunlight-induced photocatalytic effect of NiO nanowires. *Mater. Des.* **2018**, *144*, 214–221. [\[CrossRef\]](#)
148. Suresh, R.; Mangalaraja, R.V.; Mansilla, H.D.; Yáñez, J. Reduced Graphene Oxide-Based Photocatalysis. In *Green Photocatalyst*; Naushad, M., Rajendran, S., Lichtfouse, E., Eds.; Springer: Chemnitz, Germany, 2020; Volume 34, pp. 145–166. [\[CrossRef\]](#)
149. Zhou, C.; Lai, C.; Huang, D.; Zeng, G.; Zhang, C.; Cheng, M.; Hu, L.; Wan, J.; Xiong, W.; Wen, M.; et al. Highly porous carbon nitride by supramolecular preassembly of monomers for photocatalytic removal of sulfamethazine under visible light driven. *Appl. Catal. B Environ.* **2018**, *220*, 202–210. [\[CrossRef\]](#)
150. Shang, Y.; Chen, X.; Liu, W.; Tan, P.; Chen, H.; Wu, L.; Ma, C.; Xiong, X.; Pan, J. Photocorrosion inhibition and high-efficiency photoactivity of porous g-C<sub>3</sub>N<sub>4</sub>/Ag<sub>2</sub>CrO<sub>4</sub> composites by simple microemulsion-assisted co-precipitation method. *Appl. Catal. B Environ.* **2017**, *204*, 78–88. [\[CrossRef\]](#)
151. Khavar, A.H.C.; Moussavi, G.; Mahjoub, A.R.; Satari, M.; Abdolmaleki, P. Synthesis and visible-light photocatalytic activity of In<sub>2</sub>S-TiO<sub>2</sub>@rGO nanocomposite for degradation and detoxification of pesticide atrazine in water. *Chem. Eng. J.* **2018**, *345*, 300–311. [\[CrossRef\]](#)
152. Chen, P.; Zhang, Q.; Shen, L.; Li, R.; Tan, C.; Chen, T.; Liu, H.; Liu, Y.; Cai, Z.; Liu, G.; et al. Insights into the synergetic mechanism of a combined vis-RGO/TiO<sub>2</sub>/peroxodisulfate system for the degradation of PPCPs: Kinetics, environmental factors and products. *Chemosphere* **2019**, *216*, 341–351. [\[CrossRef\]](#)
153. Zhou, X.; Zhou, S.; Ma, F.; Xu, Y. Synergistic effects and kinetics of rGO-modified TiO<sub>2</sub> nanocomposite on adsorption and photocatalytic degradation of humic acid. *J. Environ. Manag.* **2019**, *235*, 293–302. [\[CrossRef\]](#)